Structural and Electronic Properties of the Tetracene/Ag(110) and Tetracene/Cu(110) Interfaces

Masterarbeit
zur Erlangung des akademischen Grades eines Master of Science an der
naturwissenschaftlichen Fakultät der Karl-Franzens-Universität Graz

vorgelegt von

Jana Fuchsberger

am Institut für Physik Fachbereich für Theoretische Physik

Betreuer: Assoz.-Prof. Dr. Peter Puschnig

Graz, 2017

Abstract

Within this thesis the geometric and electronic properties of the tetracene/Ag(110) interface and the tetracene/Cu(110) interface are studied in the framework of density functional theory. The optimal adsorption geometry is investigated for both systems using damped molecular dynamics to relax different supercells and calculate the respective adsorption energies. We further analyze the electronic structures of the energetically most favorable geometries in terms of work function modifications, charge rearrangements, projected density of states and molecular orbital projected density of states. Finally, we compare simulated photoemission momentum maps for the two systems with experimental data.

Kurzzusammenfassung

In dieser Arbeit werden die elektronischen und geometrischen Eigenschaften der Tetrazen/Ag(110) und der Tetrazen/Cu(110) Oberfläche im Rahmen der Dichtefunktionaltheorie studiert. Um die optimale Adsorptionsgeometrie zu untersuchen werden für beide Systeme mit der Hilfe von 'damped molecular dynamics' verschiedene Superzellen relaxiert und deren Adsorptionsenergien berechnet. Außerdem analysieren wir die elektronische Struktur der energetisch günstigsten Geometrien hinsichtlich der Änderung der Austrittsarbeit, der Ladungsdichteumverteilung, der projizierten Zustandsdichte und der Molekülorbital projizierten Zustandsdichte. Schließlich werden simulierte Photoemission-Impuls Karten beider Systeme mit experimentellen Daten verglichen.

Contents

1 Introduction **1**

2 Theory **3**

2.1 Quantum Mechanical Many Electron Problem 3
2.2 Density Functional Theory 4
2.2.1 Hohenberg-Kohn Theorems 4
2.2.2 Kohn-Sham Equations 5
2.2.3 Exchange-Correlation Energy Functional 7
2.3 In-Silico DFT Calculations 8
2.3.1 Plane Wave Expansion 8
2.3.2 Projector Augmented Wave Method 10
2.3.3 Calculations with the Vienna Ab-Initio Simulation Package 12
2.3.4 Simulation of a Surface 12
2.4 Simulated Photoemission Intensity 13
2.4.1 Fundamentals of Photoemission Spectroscopy 13
2.4.2 Calculation of the Photoemission Intensity 14

3 Results **17**

3.1 Adsorption Geometry 17
3.1.1 Ionic Relaxation Calculations with VASP 17
3.1.2 The Tetracene/Ag(110) Interface 18
3.1.3 The Tetracene/Cu(110) Interface 20
3.2 Density of States 23
3.2.1 The Tetracene/Ag(110) Interface 24
3.2.2 The Tetracene/Cu(110) Interface 25
3.3 Charge Rearrangements and Work Function Variations 30
3.3.1 The Tetracene/Ag(110) Interface 31
3.3.2 The Tetracene/Cu(110) Interface 33
3.4 Photoemission Momentum Maps 35
3.4.1 The Tetracene/Ag(110) Interface 35
3.4.2 The Tetracene/Cu(110) Interface 40
3.5 Comparison of the Tetracene/Ag(110) Interface to the Tetracene/Cu(110) . . 40

4 Conclusion **43**

5 Bibliography **47**

CHAPTER 1

Introduction

The general motivation to investigate organic/metal interfaces is that a good knowledge of the electronic properties of such interfaces is crucial to reach a better performance and stability in modern organic electronics.

In this work a theoretical analysis of two specific organic/metal interfaces is conducted. A theoretical viewpoint proofs useful on the one side to gather detailed knowledge, while on the other hand it can also be beneficial to better understand and interpret data from experimental research.

An organic/metal interface is a solid state system exhibiting quantum mechanical behavior and should therefore be described using the Schrödinger equation, which unfortunately can only be solved exactly for very simple problems. Thus a numerical treatment and appropriate approximations are inevitable. In this thesis we approach the problem using density functional theory (DFT), which is a formalism describing the ground state of a quantum mechanical N-electron system using only the electron density instead of the complicated N-electron wave functions. The main ideas and strategies of DFT will briefly be introduced in the first part of this thesis.

The organic material of interest in this work is tetracene, an organic semiconductor that is used building organic field-effect transistors and organic light-emitting diodes. In particular we explore the electronic properties of tetracene on two different metal surfaces with face-centered cubic crystal structure: Ag(110) and Cu(110).

Using the Vienna ab-initio simulation package (VASP) to conduct DFT calculations we start our analysis by investigating the optimal adsorption geometry of tetracene on both surfaces. Moreover we calculate the density of states and compare it to the experimental energy distribution curve (EDC) to gain insight about molecular orbital positions. Consequently we analyze the rearrangement of charge upon adsorption of tetracene on both surfaces as well as the work function variations, which are especially important when it comes to technical applications of organic/metal interfaces. To gather additional knowledge about the nature about the molecular orbitals of both interfaces we visualize them in k-space by simulating photoemission momentum maps and then compare them to their experimental counterparts.

CHAPTER 2

Theory

2.1 Quantum Mechanical Many Electron Problem

The fundamental equation to describe materials from a quantum mechanical point of view is the Schrödinger equation. Therefore we need to write down the Hamiltonian of our system. In this description we group the constituents of a solid into valence electrons e and lattice ions i, considering that core electrons are tightly bound to the nucleus, while valence electrons contribute to chemical bonding and therefore have a major influence on the properties of the material.

$$\hat{H} = \hat{T}_e + \hat{T}_i + \hat{V}_{i-i} + \hat{V}_{e-i} + \hat{V}_{e-e} \tag{2.1}$$

This is the so called molecular Hamiltonian [1], which consists of the kinetic energy of the electrons and the kinetic energy of the ions, as well as the electron-electron, ion-ion and electron-ion interaction.

Due to the huge mass difference between electrons and ions one can assume, that the electrons follow the lattice ions instantaneously. Therefore following the well known Born-Oppenheimer approximation, the electronic dynamics can be separated from the ionic dynamics. The coordinates of the lattice ions are consequently regarded as parameters for the electronic problem. In the resulting Hamiltonian for N electrons the lattice ions contribute in the form of an external potential

$$\hat{H} = \underbrace{-\frac{1}{2}\sum_{i=1}^{N} \Delta_i}_{\hat{T}_e} + \underbrace{\sum_{i=1}^{N} v(\boldsymbol{r}_i)}_{\hat{V}_{ext}} + \underbrace{\frac{1}{2}\sum_{j\neq i}^{N} \frac{e^2}{|\boldsymbol{r}_i - \boldsymbol{r}_j|}}_{\hat{V}_{e-e}} \tag{2.2}$$

Now we can write down the stationary Schrödinger equation for a system with the complete set of quantum numbers k.

$$\hat{H}\psi_k(\boldsymbol{r}_1\sigma_1, \boldsymbol{r}_2\sigma_2, \ldots, \boldsymbol{r}_N\sigma_N) = E_k\psi_k(\boldsymbol{r}_1\sigma_1, \boldsymbol{r}_2\sigma_2, \ldots, \boldsymbol{r}_N\sigma_N) \tag{2.3}$$

The wave functions ψ are antisymmetric under the exchange of two electrons and fulfill the normalization condition

$$\sum_{\sigma_1} \cdots \sum_{\sigma_N} \int d^3r_1 \cdots d^3r_N |\psi_k(\boldsymbol{r}_1\sigma_1, \boldsymbol{r}_2\sigma_2, \ldots, \boldsymbol{r}_N\sigma_N)|^2 = \langle\psi_k|\psi_k\rangle = 1 \tag{2.4}$$

The electrons in the wave function are indistinguishable, hence the expression

$$N!|\psi_k(\boldsymbol{r}_1\sigma_1, \boldsymbol{r}_2\sigma_2, \ldots, \boldsymbol{r}_N\sigma_N)|^2 d^3r_1 \ldots d^3r_N \tag{2.5}$$

gives the probability of finding any electron with spin σ_1 in d^3r_1 and any electron with spin σ_2 in d^3r_2 and so on. The full wave function depends on the coordinates and spins of all N electrons and consequently has $3N$ dimensions. For solid state systems, which contain a huge number of electrons (around 10^{23}), handling such high dimensional wave functions is impossible due to an exponential scaling with N. Another equally interesting but much more convenient physical quantity is the 3-dimensional electron spin density. It is defined, so that $n_\sigma(\boldsymbol{r})d^3r$ is the probability of finding an electron with the spin σ in d^3r at $\boldsymbol{r}$. [2]

$$n_\sigma(\boldsymbol{r}) = N \sum_{\sigma_1 \ldots \sigma_N} \int d^3r_2 \ldots \int d^3r_N \, |\psi_k(\boldsymbol{r}_1\sigma_1, \boldsymbol{r}_2\sigma_2, \ldots, \boldsymbol{r}_N\sigma_N)|^2 \tag{2.6}$$

From 2.4 and 2.6 it follows that

$$\sum_\sigma \int d^3r \, n_\sigma(\boldsymbol{r}) = N. \tag{2.7}$$

2.2 Density Functional Theory

Density functional theory (DFT) is a theory used to describe the ground state of a many electron system based on the idea to use the electron spin density instead of the full wave function. Two theorems by Hohenberg and Kohn build the proper mathematical basis for DFT, they will be discussed in the following.

2.2.1 Hohenberg-Kohn Theorems

To discuss the Hohenberg-Kohn theorems, we follow the constrained search approach by Levy [3] instead of performing the *reductio ad absurdum* proof as it was done originally by Hohenberg and Kohn [4]. As a starting point we take the wave function variational principle, which tells us that minimizing $\langle\psi|\hat{H}|\psi\rangle$ over all normalized many electron wave functions yields the ground state energy:

$$E_0 = \min_\psi \langle\psi|\hat{H}|\psi\rangle \tag{2.8}$$

Subsequently we split the task into two steps:

1. minimize with respect to the wave functions
2. minimize with respect to the density

Starting by minimizing over all wave functions that give the same fixed electron density yields the total energy functional:

$$
\begin{aligned}
E[n] &= \min_{\psi\to n} \langle\psi|\hat{H}|\psi\rangle && (2.9)\\
&= \min_{\psi\to n} \langle\psi|\hat{T}+\hat{V}_{ext}+\hat{V}_{e-e}|\psi\rangle && (2.10)\\
&= \min_{\psi\to n} \langle\psi|\hat{T}+\hat{V}_{e-e}|\psi\rangle + \int v(\boldsymbol{r})n(\boldsymbol{r})d^3r && (2.11)
\end{aligned}
$$

The first term in 2.11 does not depend on the specific system and is therefore called the universal functional:

$$F[n] \equiv \min_{\psi\to n} \langle\psi|\hat{T}+\hat{V}_{e-e}|\psi\rangle \tag{2.12}$$

Hohenberg-Kohn Theorem 1 *The ground-state energy of a system of interacting electrons as described by the Schrödinger equation is a unique functional of the total electron density. [4]*

In the second step one can now calculate the ground state energy by minimizing the total energy functional over all electron densities, that give the same number of electrons.

$$E_0 = \min_n E[n] = \min_n \left\{F[n] + \int v(\boldsymbol{r})n(\boldsymbol{r})d^3r\right\} \tag{2.13}$$

Hohenberg-Kohn Theorem 2 *The electron density that minimizes the energy of the overall functional is the true electron density corresponding to the full solution of the Schrödinger equation. [4]*

The minimization is carried out under the constraint of a fixed electron number N. Using the technique of Lagrange multipliers one obtains

$$\delta\{F[n] + \int d^3r v(\boldsymbol{r})n(\boldsymbol{r}) - \mu \underbrace{\int n(\boldsymbol{r})d^3r\}}_{=N} \overset{!}{=} 0 \tag{2.14}$$

where μ is the Lagrange multiplier. The resulting Euler equation reads

$$\frac{\delta F[n]}{\delta n(\boldsymbol{r})} + v(\boldsymbol{r}) = \mu. \tag{2.15}$$

2.2.2 Kohn-Sham Equations

Although the Hohenberg-Kohn theorems reveal important properties about the electron density of a system, they do not provide a method to calculate the ground state density.

For the purpose of developing a scheme, that can be applied in practice, Kohn and Sham proposed to consider an auxiliary non-interacting system of electrons [5], hence the electron-electron potential vanishes. This system should be constructed in such a way, that it gives the same density as the corresponding system where the electrons interact with each other. The new Hamiltonian of this auxiliary system reads

$$\hat{H}^S = \hat{T} + \hat{V}^S_{ext} \tag{2.16}$$

Minimizing over all wave functions that give the same fixed electron density gives

$$E[n] = \min_{\phi \to n} \langle \phi | \hat{H}^S | \phi \rangle = \min_{\phi \to n} \underbrace{\langle \phi | \hat{T} | \phi \rangle}_{T_S[n]} + \int n(\boldsymbol{r}) v_S(\boldsymbol{r}) d^3 r \tag{2.17}$$

Here we have introduced the functional $T_S[n]$, which describes the kinetic energy of a system of independent electrons. Note that ϕ is, unlike the N-electron wave function ψ of the interacting system, only a single Slater determinant of single particle wave functions φ_i.

The second minimization step with respect to the density, including the constraint $\int n(\boldsymbol{r}) d^3 r = N = \text{const.}$, results in

$$\frac{\delta T_S[n]}{\delta n(\boldsymbol{r})} + v_S(\boldsymbol{r}) = \mu \tag{2.18}$$

The universal functional $F[n]$, like suggested by Kohn and Sham is given below

$$F[n] = T_S[n] + U[n] + E_{xc}[n] \tag{2.19}$$

$U[n]$ is the Hartree energy and $E_{xc}[n]$ is the exchange-correlation energy, which is basically defined to include everything that the other terms in 2.19 are lacking, but this will be discussed in more detail in 2.2.3. In order to achieve that the Euler equations 2.15 and 2.18 are equivalent the Kohn-Sham potential $v_S(\boldsymbol{r})$ must take the following form

$$v_S(\boldsymbol{r}) = v(\boldsymbol{r}) + v_H(\boldsymbol{r}) + v_{xc}(\boldsymbol{r}) \tag{2.20}$$

where

$$v_H(\boldsymbol{r}) = \frac{\delta U[n]}{\delta n} = \int \frac{n(\boldsymbol{r}')}{|\boldsymbol{r} - \boldsymbol{r}'|} d^3 r' \tag{2.21}$$

is the Hartree potential and

$$v_{xc}(\boldsymbol{r}) = \frac{\delta E_{xc}[n]}{\delta n} \tag{2.22}$$

is the exchange correlation potential.

Now we can write down the Kohn-Sham equations, which are single particle Schrödinger equations.

$$\left[-\frac{1}{2}\Delta + v_S(\boldsymbol{r})\right]\varphi_i(\boldsymbol{r}) = \varepsilon_i\varphi_i(\boldsymbol{r}) \tag{2.23}$$

The energies ε_i are called Kohn-Sham energies and the single-particle wave functions $\varphi_i(\boldsymbol{r})$ Kohn-Sham orbitals. In our auxiliary system of non-interacting electrons the N-electron wave function ϕ is a Slater determinant consisting of single-particle wave functions φ_i, therefore one can express the density in a very simple form

$$n(\boldsymbol{r}) = \sum_{i=1}^{N} |\varphi_i(\boldsymbol{r})|^2 \tag{2.24}$$

2.2.3 Exchange-Correlation Energy Functional

In the previous chapter the exchange-correlation energy functional has been introduced as the quantity that includes all physical effects, that are not covered by the other terms in the total energy functional. No analytical form of E_{xc}, where no unknown quantities remain, has yet been discovered, hence an approximation must be used. Such an approximation should account for:

1. self interaction correction (over counted in Hartree energy)
2. Pauli principle
3. Coulomb correlations of electrons

Nonetheless we can split the exchange-correlation energy functional in its two main parts

$$E_{xc}[n] = E_x[n] + E_c[n] \tag{2.25}$$

where the exchange part is defined as

$$E_x[n] \equiv \langle \phi_n^{min} | \hat{V}_{e-e} | \phi_n^{min} \rangle - U[n] \tag{2.26}$$

In consequence the correlation part is

$$E_c[n] = E_{xc}[n] - E_x[n] = \langle \psi_n^{min} | \hat{T} + \hat{V}_{e-e} | \psi_n^{min} \rangle - \langle \phi_n^{min} | \hat{T} + \hat{V}_{e-e} | \phi_n^{min} \rangle \tag{2.27}$$

Recalling 2.19 we notice that ψ_n^{min} is the wave function that yields the density n and minimizes $\langle \hat{T} + \hat{V}_{e-e} \rangle$ and from 2.17 we know that ϕ_n^{min} is the wave function that yields the density n and minimizes $\langle \hat{T} \rangle$, thus

$$E_c[n] < 0 \tag{2.28}$$

Working out a good approximation of the exchange-correlation energy functional is one of the main difficulties in DFT. The simplest approximation is the local density approximation (LDA)

$$E_{xc}^{LDA} = \int n(\boldsymbol{r}) e_{xc}^{unif}(n(\boldsymbol{r})) d^3r \tag{2.29}$$

$$e_{xc}^{unif}(n(\boldsymbol{r})) = e_x(n(\boldsymbol{r})) + e_c(n(\boldsymbol{r})) \tag{2.30}$$

In a uniform electron gas the density can be written in terms of r_S the Wigner-Seitz radius, which is the radius of a sphere that on average contains one electron.

$$n = \frac{3}{4\pi r_S^3} \tag{2.31}$$

Using this result the exchange energy per electron can be calculated

$$e_x(n(\boldsymbol{r})) = -\left(\frac{3}{2\pi}\right)^{\frac{2}{3}} \frac{3}{4r_S} \tag{2.32}$$

For the correlation energy per electron analytic expressions are only known for the high density limit ($r_S \to 0$) [6] and the low density limit ($r_S \to \infty$) . For intermediate cases the correlation energy per electron can be computed using quantum Monte-Carlo methods [7].

A more sophisticated approximation is the general gradient approximation (GGA), which unlike the LDA also includes the gradient of the density and can be written like [8]

$$E_{xc}^{GGA}[n] = \int f(n(\boldsymbol{r}), \nabla n(\boldsymbol{r})) d^3r \tag{2.33}$$

GGA's can be considered *semi*local and in contrast to LDA there is no universal form, but many different kinds of GGA.

2.3 In-Silico DFT Calculations

2.3.1 Plane Wave Expansion

In order to perform calculations one has to choose an appropriate set of basis functions. In the case of translational symmetry, plane wave functions are the best choice, because they are orthonormal, complete and lattice periodic and thus obey Bloch's theorem.

$$\phi_{\boldsymbol{k}+\boldsymbol{G}}(\boldsymbol{r}) = \frac{1}{\sqrt{\Omega}} e^{i(\boldsymbol{k}+\boldsymbol{G})\boldsymbol{r}} \tag{2.34}$$

Here $\boldsymbol{k}$ is the Bloch vector, $\boldsymbol{G}$ is a reciprocal lattice vector and Ω is the crystal volume. Expanding the Kohn-Sham orbitals into plane waves yields

$$\varphi_{n\boldsymbol{k}}(\boldsymbol{r}) = \frac{1}{\sqrt{\Omega}} e^{i\boldsymbol{k}\boldsymbol{r}} \sum_{\boldsymbol{G}'} c_{n\boldsymbol{k}}(\boldsymbol{G}') e^{i\boldsymbol{G}'\boldsymbol{r}} \tag{2.35}$$

Inserting the expansion into the Kohn-Sham equations, we find the following matrix eigenvalue equation

$$\sum_{\boldsymbol{G}'} H_{\boldsymbol{G}\boldsymbol{G}'}(\boldsymbol{k}) c_{n\boldsymbol{k}}(\boldsymbol{G}') = \varepsilon_{n\boldsymbol{k}} c_{n\boldsymbol{k}}(\boldsymbol{G}') \tag{2.36}$$

For the Hamiltonian matrix element one finds

$$H_{\boldsymbol{G}\boldsymbol{G}'}(\boldsymbol{k}) = \frac{|\boldsymbol{k}+\boldsymbol{G}|^2}{2} \delta_{\boldsymbol{G}\boldsymbol{G}'} + \frac{1}{\Omega} \tilde{v}(\boldsymbol{G}-\boldsymbol{G}') \tag{2.37}$$

Here $\tilde{v}(\boldsymbol{G}-\boldsymbol{G}')$ is the Fourier transform of the Kohn-Sham potential. The kinetic energy term naturally is diagonal since plane waves are eigenfunctions of the free electron.

Strictly speaking the plane wave expansion of Eq. 2.35 includes a sum over an infinite number of reciprocal lattice vectors $\boldsymbol{G}$. Since in practice one has to use a finite number of basis functions, we have to establish a cut-off for all numerical applications

$$E_{cut} = \frac{1}{2} \boldsymbol{G}_{max}^2 \tag{2.38}$$

The following flow chart demonstrates how to put the self-consistent solution of the Kohn-Sham equations into practice using a plane wave expansion.

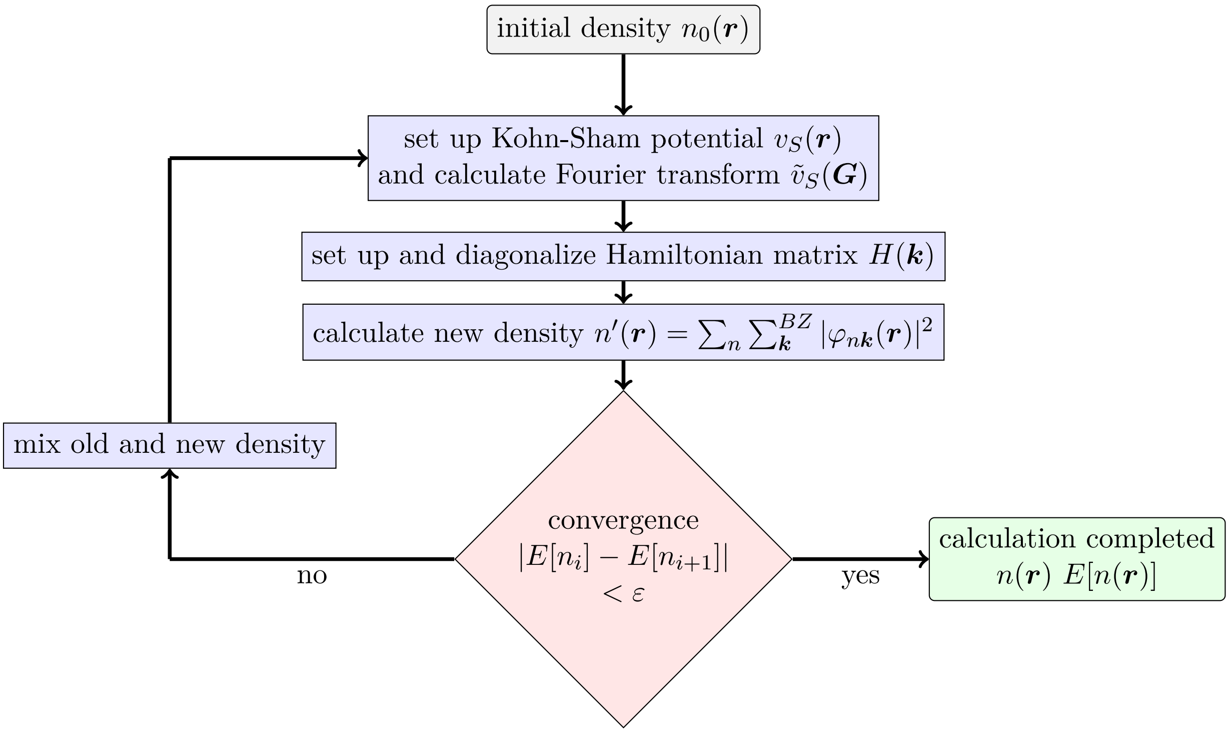
initial density $n_0(\boldsymbol{r})$
set up Kohn-Sham potential $v_S(\boldsymbol{r})$ and calculate Fourier transform $\tilde{v}_S(\boldsymbol{G})$
set up and diagonalize Hamiltonian matrix $H(\boldsymbol{k})$
calculate new density $n'(\boldsymbol{r}) = \sum_n \sum_{\boldsymbol{k}}^{BZ} |\varphi_{n\boldsymbol{k}}(\boldsymbol{r})|^2$
convergence $|E[n_i] - E[n_{i+1}]| < \varepsilon$
no
mix old and new density
yes
calculation completed $n(\boldsymbol{r})$ $E[n(\boldsymbol{r})]$

Figure 2.1: Self-consistent solution of Kohn-Sham equations

2.3.2 Projector Augmented Wave Method

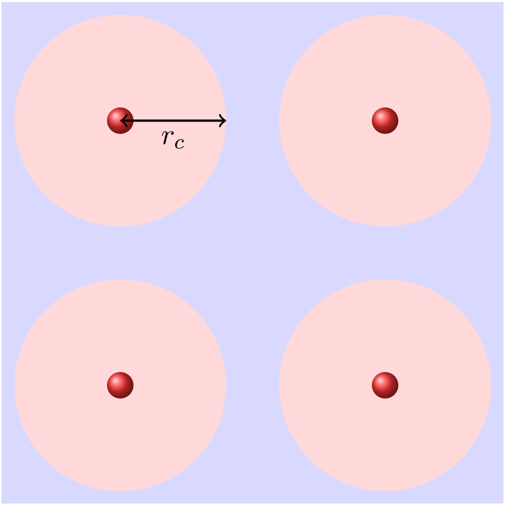

Fig. 2.2: Schematic illustration of the augmentation region (red) and the interstitial region (blue)

The chosen basis set of plane wave functions works really well in the bonding region between the lattice ions, where the potential is smooth and the wave functions are plane-wave like. In the region near the lattice ions however the kinetic energy is high, which causes the wave function to oscillate strongly. This behavior is easily described by a product of a few spherical harmonics and radial wave functions, but the plane wave expansion converges very slowly. This problem can be cured using the projector augmented wave method (PAW) [9, 10]. The PAW method distinguishes between the region near the lattice ions ($|\boldsymbol{r}| < r_c$) as seen in Fig. 2.2, called augmentation region and the interstitial region. In the augmentation region an auxiliary wave function $|\tilde{\varphi}\rangle$ is used. It has a rapidly convergent plane wave expansion and is related to the true wave function $|\varphi\rangle$ through a transformation $\mathcal{T}$

operator

$$|\varphi\rangle = \mathcal{T}\,|\tilde{\varphi}\rangle \tag{2.39}$$

In the augmentation region the auxiliary wave function can be decomposed into auxiliary partial waves

$$|\tilde{\varphi}\rangle = \sum_i c_i\,|\tilde{\alpha}_i\rangle \tag{2.40}$$

with coefficients

$$c_i = \langle\tilde{p}_i|\tilde{\varphi}\rangle \tag{2.41}$$

The $|\tilde{p}_i\rangle$ are called projector functions. Together with the auxiliary partial waves they have to fulfill the following orthogonality relation in the augmentation region

$$\langle\tilde{p}_i|\tilde{\alpha}_i\rangle = \delta_{ij} \tag{2.42}$$

The transformation operator $\mathcal{T}$ can be written

$$\mathcal{T} = 1 + \sum_i \left(|\alpha_i\rangle - |\tilde{\alpha}_i\rangle\right)\langle\tilde{p}_i| \tag{2.43}$$

So for the full wave function it follows

$$|\varphi\rangle = |\tilde{\varphi}\rangle \underbrace{- \sum_i \langle\tilde{p}_i|\tilde{\varphi}\rangle\,|\tilde{\alpha}_i\rangle}_{\mathrm{I}} \underbrace{+ \sum_i \langle\tilde{p}_i|\tilde{\varphi}\rangle\,|\alpha_i\rangle}_{\mathrm{II}} \tag{2.44}$$

By means of the projector functions the term I removes the non-physical part from the auxiliary wave function, while the term II adds the required physical part to end up with the true wave function. Equivalent to 2.2.3 the variational principle yields Schrödinger-like equations for a set of auxiliary wave functions

$$\mathcal{T}^\dagger \hat{H} \mathcal{T}\,|\tilde{\varphi}_n\rangle = \varepsilon_n \mathcal{T}^\dagger \mathcal{T}\,|\tilde{\varphi}_n\rangle \tag{2.45}$$

Expectation values can now be obtained either from the auxiliary wave functions directly, or from the reconstructed physical wave functions

$$\langle \hat{A} \rangle = \sum_n f_n \langle \varphi_n | \hat{A} | \varphi_n \rangle + \sum_{n=1}^{N_c} \langle \varphi_n^c | \hat{A} | \varphi_n^c \rangle \tag{2.46}$$

$$= \sum_n f_n \langle \tilde{\varphi_n} | \mathcal{T}^\dagger \hat{A} \mathcal{T} | \tilde{\varphi_n} \rangle + \sum_{n=1}^{N_c} \langle \varphi_n^c | \hat{A} | \varphi_n^c \rangle \tag{2.47}$$

Here f_n are the occupations of valence states, $|\varphi_n^c\rangle$ are the core states and N_c is the number of core states.

2.3.3 Calculations with the Vienna Ab-Initio Simulation Package

All calculations in this work were realized using the Vienna Ab-Initio Simulation Package (VASP) [11–13], which is a program package applicable for ab-initio electronic structure calculations and quantum-mechanical molecular dynamics.

The Kohn-Sham orbitals, electron charge density and local potential are expanded in a plane wave basis set utilizing the PAW method.

To solve the Kohn-Sham matrix equation 2.36 by matrix diagonalization VASP uses the residual minimization method with direct inversion of the iterative subspace (RMM-DIIS) or blocked Davidson algorithms.

VASP offers different exchange correlation functionals: LDA, GGAs and meta GGAs. In this work the exchange correlation functional found by J. P. Perdew, K. Burke and M. Ernzerhof [14] (PBE) was used. The PBE functional retains correct features of the local spin density approximation (LSDA), an extension of LDA 2.29 to spin-polarized systems, and adds the energetically most important features of gradient-corrected nonlocality. One should consider, that equilibrium distances are usually overestimated while vibrational frequencies are mostly underestimated by PBE.

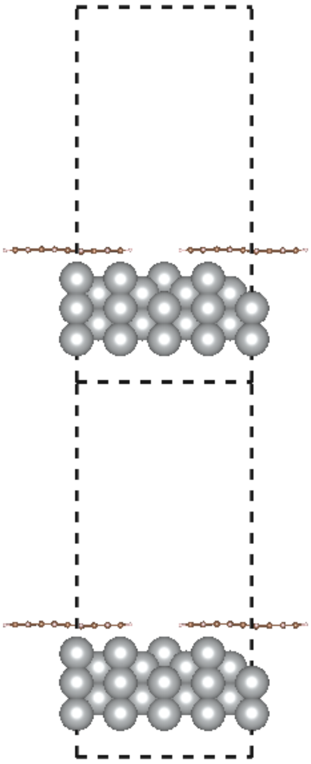

Fig. 2.3: Slab model: side view of 2 supercells

Nonetheless the PBE functional (nor a LDA or any other GGA functional for that matter) is not able to accurately describe long-range van der Waals interactions. For this reason the Tkatchenko-Scheffler method [15] was used for Van der Waals corrections.

2.3.4 Simulation of a Surface

In this work sufaces of two different materials are investigated: silver and copper. Both materials are crystals and hence best described using a so-called supercell and periodic boundary conditions. How does one describe a surface using periodic boundary conditions? One way to do it is the slab model [16], like pictured in 2.3. The slab model applies periodic boundary conditions in all three dimensions and the supercell is built in a way that the resulting simulated system is a series of stacked slabs of the solid separated by a vacuum slab. It is important to choose the thickness of the vacuum layer and the number of crystal layers wisely:

- The vacuum has to be large enough to prevent the crystal surface of one supercell to interact with the bottom of the crystal in the next supercell. To guarantee, that this is the case the charge density has to be close to zero in the vacuum slab.
- In a face-centered cubic (fcc) material (like Ag or Cu) the distance between two adjacent layers in the bulk is constant. This is not true at the surface: For top layers of the material it is energetically more favorable to alter their z-positions from the ideal bulk positions. This phenomenon is called surface relaxation. Therefore one has to simulate enough layers, so that surface relaxation does not depend on the number of simulated layers, to get realistic results.

A supercell is described using three lattice vectors: One in z-direction defining the height and two vectors in x- and y-direction respectively describing the shape of the cell in the plane of the interface. As soon as we put molecules on a surface these x- and y-direction lattice vectors ($\boldsymbol{a}_{\text{overlayer}}$ and $\boldsymbol{b}_{\text{overlayer}}$) have to be larger than the original x- and y-direction unit vectors of the surface material ($\boldsymbol{a}_{\text{surf}}$ and $\boldsymbol{b}_{\text{surf}}$) in order to fit the molecules in the new cell, which is called overlayer cell and describe the desired geometry. This overlayer cell is commonly described using the so-called epitaxial matrix A:

$$\begin{pmatrix} \boldsymbol{a}_{\text{overlayer}} \\ \boldsymbol{b}_{\text{overlayer}} \end{pmatrix} \underbrace{\begin{pmatrix} A_{11} & A_{12} \\ A_{21} & A_{22} \end{pmatrix}}_{\boldsymbol{A}} = \begin{pmatrix} \boldsymbol{a}_{\text{surf}} \\ \boldsymbol{b}_{\text{surf}} \end{pmatrix} \tag{2.48}$$

2.4 Simulated Photoemission Intensity

2.4.1 Fundamentals of Photoemission Spectroscopy

Photoemission Spectroscopy is a highly useful experimental technique based on the photoelectric effect, which was first measured by Hallwachs in 1888 following earlier observations by Hertz. The theoretical explanation was given 17 years later by Einstein using the hypothesis of light quanta [17]. A so-called photoelectron is emitted when an incoming photon with energy $\hbar\omega$ is absorbed by the solid. We can write the energy of the photoelectron as

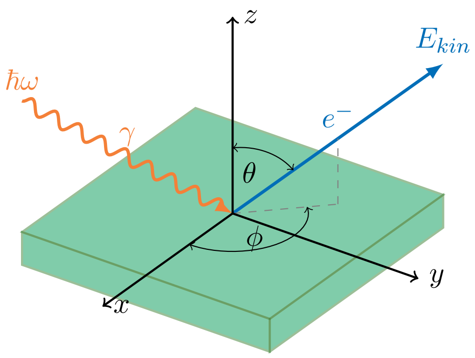

Fig. 2.4: Schematic illustration of photoemission spectroscopy

$$E_{kin} = \hbar\omega - E_B = \hbar\omega - \varPhi - E_i \quad (2.49)$$

Here E_B denotes the binding energy, which consists of the work function $\varPhi$ and E_i the energy of the photoelectron's initial state with respect to the Fermi energy. This means, that we can gather information about the electronic structure of a system interpreting the intensity resulting from photoemission spectroscopy.

2.4.2 Calculation of the Photoemission Intensity

One can describe the photoemission intensity using the one-step-model [18, 19], which is illustrated in 2.5. The one-step-model describes the photoemission process as a transition from an electronic bound state to an electronic continuum state due to excitation caused by an incoming photon.

The photoemission intensity can be written as a Fermi's golden rule like expression containing a sum over all transition probabilities from the initial states $|\varPsi_i\rangle$ to the desired final state $|\varPsi_f(\theta,\phi;E_{kin})\rangle$, which is characterized by the direction (θ,ϕ) and the kinetic energy of the photoelectron, times a δ-function ensuring energy conservation.

$$I(\theta,\phi;E_{kin}) \propto \\ \sum_i |\langle\varPsi_f(\theta,\phi;E_{kin})|\,\boldsymbol{A}\cdot\boldsymbol{p}+\boldsymbol{p}\cdot\boldsymbol{A}\,|\varPsi_i\rangle|^2 \times \delta(E_i+\varPhi+E_{kin}-\hbar\omega) \tag{2.50}$$

For our application the quadratic term in $\boldsymbol{A}$ is negligable and hence was dropped in this description. Furthermore we now assume dipole approximation, which holds sufficiently well, because the wavelength of ultraviolet light is much lager than common lattice constants. The dipole approximation ($\boldsymbol{A} \approx const.$) causes the following commutation relation to vanish

$$[\boldsymbol{A},\boldsymbol{p}] = i\hbar\nabla\boldsymbol{A} = 0 \tag{2.51}$$

and simplyfies the photon electron interaction to

$$\frac{1}{2}(\boldsymbol{A}\cdot\boldsymbol{p}+\boldsymbol{p}\cdot\boldsymbol{A}) = \boldsymbol{p}\cdot\boldsymbol{A}. \tag{2.52}$$

Additionally we approximate the final state $|\varPsi_f(\theta,\phi;E_{kin})\rangle$ by a plane wave and hereby neglect spherical scattering effects of the outgoing wave. Applying both approximations to 2.50 yields

$$I(k_x,k_y;E_{kin}) \propto |\boldsymbol{A}\cdot\boldsymbol{k}|^2 \sum_i |\langle e^{i\boldsymbol{k}\boldsymbol{r}}|\varPsi_i\rangle|^2 \times \delta(E_i+\varPhi+E_{kin}-\hbar\omega) \tag{2.53}$$

In this formulation the photoemission intensity is proportional to the Fourier transform of the initial state times the polarization factor $|\boldsymbol{A} \cdot \boldsymbol{k}|^2$. As an input for the simulated photoemission intensity the Kohn-Sham orbitals φ_i and energies ε_i can be used. This is an approximation, which has turned out to yield satisfying results for many organic/metal interfaces [21].

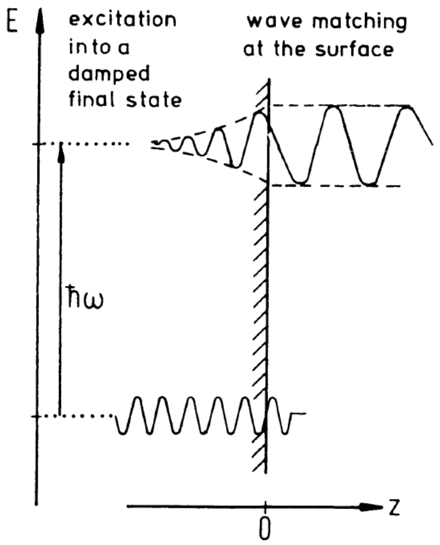
E
excitation into a damped final state
wave matching at the surface
ħω
z
0

Fig. 2.5: Schematic illustration of the one-step model (from [20])

CHAPTER 3

Results

In this section the results are presented. All calculations were conducted using VASP [11–13] and the resulting data was processed using PYTHON and MATLAB as well as VESTA and xmgrace for visual processing.

3.1 Adsorption Geometry

As a first step we investigate the adsorption geometry of both systems, the tetracene/Ag(110) and the tetracene/Cu(110) interface. The correct adsorption geometry serves as a basis for all other calculations and analysis.

3.1.1 Ionic Relaxation Calculations with VASP

The adsorption geometry is the optimal geometry for the combined system and can therefore be found by minimizing the energy with respect to different positions of the lattice ions in the super cell. VASP includes different algorithms to perform such an ionic relaxation. The ionic relaxation method used in this work is damped molecular dynamics, which can be activated setting the *IBRION* flag in the VASP input file *INCAR* to 3 ($IBRION = 3$). The positions and velocities of the lattice ions are updated in every ionic relaxation step according to the following damped second order equation of motion, which is describing intermolecular forces [22, 23].

$$\ddot{\boldsymbol{x}} = -2\alpha \boldsymbol{F} - \mu \dot{\boldsymbol{x}} \tag{3.1}$$

VASP uses the velocity Verlet method to implement 3.1:

$$\boldsymbol{v}_{N+\frac{1}{2}} = \frac{1}{1+\mu/2}\left(\left(1-\frac{\mu}{2}\right)\boldsymbol{v}_{N-\frac{1}{2}} - 2\alpha \boldsymbol{F}_N\right) \tag{3.2}$$

$$\boldsymbol{x}_{N+1} = \boldsymbol{x}_{N+1} + \boldsymbol{v}_{N+\frac{1}{2}} \tag{3.3}$$

$\boldsymbol{F}_N$ are the current forces, while the damping factor μ and the time step α must be specified in the *INCAR* file using the flags *SMASS* and *POTIM*. In order to stop the ionic relaxation calculation a break condition must be met: All forces must be smaller than *EDIFFG*, which is like the other parameters set in the *INCAR* file.

In this work the following values were used:

- damping factor μ : $SMASS = 0.4$
- time step α : $POTIM = 0.15$
- break condition: $EDIFFG = 10^{-2}\frac{eV}{\text{Å}}$

Depending on the initial configuration of the super cell it is possible that the ionic relaxation calculation settles only for a local minimum in total energy instead of the global minimum. For this reason one considers various starting geometries, described by possibly different supercells, that are likely to describe the ideal adsorption geometry and compares them. If the cells contain the same number of atoms one can directly compare the respective total energies. Is this not the case, one has to calculate the adsorption energy, which is defined as

$$E_{\text{ad}} = E_{\text{mol}} + E_{\text{surf}} - E_{\text{mol/surf}} \tag{3.4}$$

where E_{mol} is the total energy of the isolated molecule, E_{surf} is the energy of the substrate surface and $E_{\text{mol/surf}}$ is the energy of the molecule/substrate interface.

3.1.2 The Tetracene/Ag(110) Interface

In this section we investigate two adsorption sites for tetracene on the Ag(110) surface and compare them to literature [24]. Ag is an fcc crystal, hence the Ag(110) surface is characterized by its close-packed rows, which can be seen in Figs. 3.1 or 3.2. Most likely tetracene adsorbs either parallel to these close-packed rows (along the $[1\bar{1}0]$ axis) or perpendicular to them (along the [001] axis). For this reason, we use two overlayer structures defined by the following epitaxial matrices:

- parallel orientation:

$$\boldsymbol{A}_{\parallel} = \begin{pmatrix} 6 & 0 \\ 0 & 3 \end{pmatrix} \tag{3.5}$$

- perpendicular orientation:

$$\boldsymbol{A}_{\perp} = \begin{pmatrix} 4 & 0 \\ 0 & 4 \end{pmatrix} \tag{3.6}$$

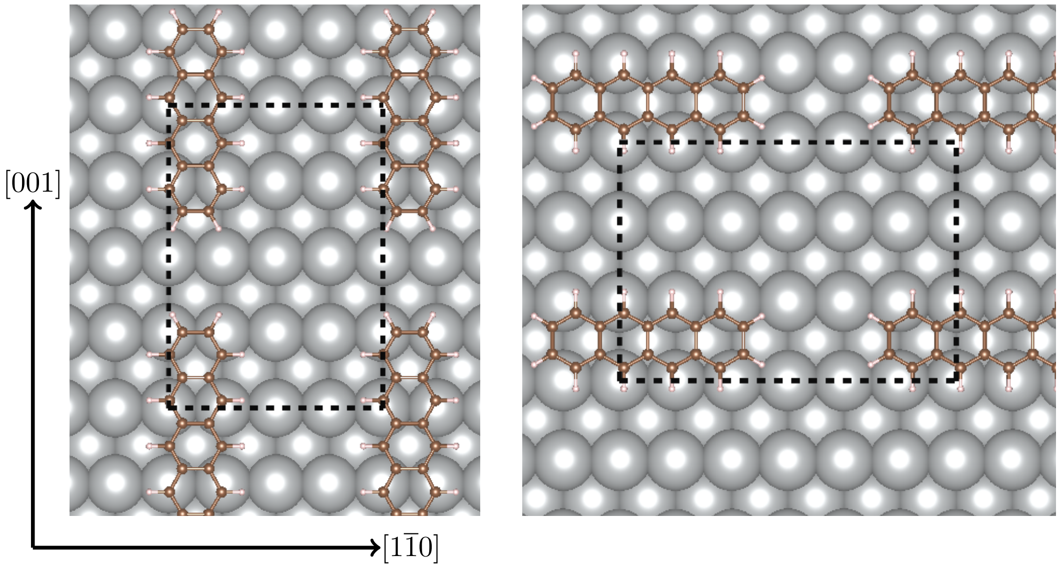

Figure 3.1: Relaxed super cells for the tetracene/Ag(110) interface, *left*: $\boldsymbol{A}_\perp$, *right*: $\boldsymbol{A}_\parallel$

In Fig. 3.1 the relaxed supercells, which have been obtained using damped molecular dynamics, are pictured for both orientations. Table 3.1 shows a comparison of the calculated adsorption energies to values from literature [24]. We note:

- The adsorption energies for the parallel and the perpendicular orientation differ only slightly, in the present calculation (approx. 80 meV) and the literature (approx. 70 meV).
- The present calculations suggest that the parallel orientation is favorable while literature suggests, that the perpendicular orientation is favorable.

Table 3.1: Comparison of adsorption energies for different super cells of the tetracene/Ag(110) interface

	parallel	perpendicular
calculated adsorption energy	2.12 eV	2.04 eV
adsorption energy from literature [24]	2.21 eV	2.28 eV

Since the energy difference between the parallel and perpendicular orientation is quite small and because of the inherent approximations in the DFT calculations (E_{xc} functional, Van der Waals corrections), a definite statement about the actual adsorption geometry is difficult. Fortunately there is more that one possibility to determine how the molecule is oriented on the surface and we will come back to this question in Section 3.4.1.

For now we examine the two adsorption geometries more closely and for this purpose take a look at the side view of the super cells. In Fig. 3.2 we see that in both cases the tetracene molecule lies almost flat on the surface and its geometry is only sightly different from the geometry of tetracene in the gas phase. Additionally the adsorption height is almost identical for both adsorption orientations, as it can be seen from Table 3.2.

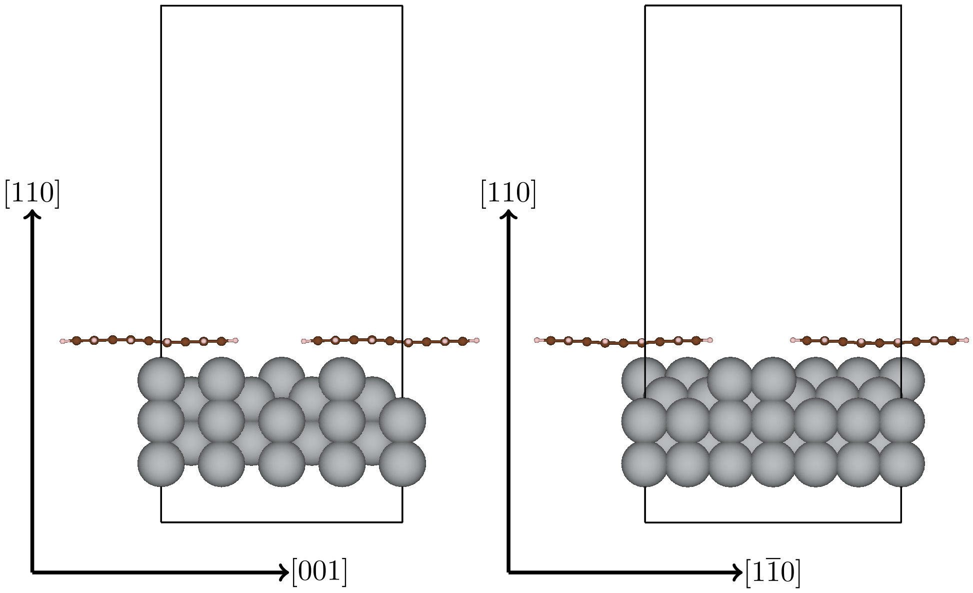

Figure 3.2: Side view of the relaxed supercells for the tetracene/Ag(110) interface, *left*: $\boldsymbol{A}_{\perp}$, *right*: $\boldsymbol{A}_{\|}$

Table 3.2: Comparison of adsorption height for different supercells of the tetracene/Ag(110) interface

	$\boldsymbol{A}_{\|}$	$\boldsymbol{A}_{\perp}$
adsorption height	2.51 Å	2.52 Å

3.1.3 The Tetracene/Cu(110) Interface

The Cu(110) surface is, like the Ag(110) surface, characterized by close-packed rows due to the fcc crystal structure, whereas the main difference between both surfaces is the considerably smaller lattice constant of Cu ($a_{Cu} \approx 3.63$Å while $a_{Ag} \approx 4.12$Å).

Literature [25, 26] states consistently, that tetracene adsorbs parallel to the close-packed rows on a Cu(110) surface, but there is no agreement on which adsorption site is favored or how the tetracene molecules are orientated on the surface with regard to each other. In this work we investigate all four high-symmetry adsorption sites for the two most likely adsorption patterns respectively. The two investigated adsorption patterns are depicted in Fig. 3.3. Either way the tetracene molecule is oriented along the [1$\bar{1}$0] axis, but in one case the molecules are arranged side by side (Fig. 3.3 *right*) while in the other case they are shifted, so that a chess board like pattern is formed (Fig. 3.3 *left*). We chose the chess board pattern super cell to be skew-angled in order to make it smaller. The corresponding epitaxial matrices are:

- chess board pattern:

$$\boldsymbol{A}_1 = \begin{pmatrix} 5 & 1 \\ 0 & 2 \end{pmatrix} \tag{3.7}$$

- square pattern:

$$\boldsymbol{A}_2 = \begin{pmatrix} 5 & 0 \\ 0 & 2 \end{pmatrix} \tag{3.8}$$

Conveniently both supercells contain the same number of atoms, thus we can directly compare total energies instead of adsorption energies.

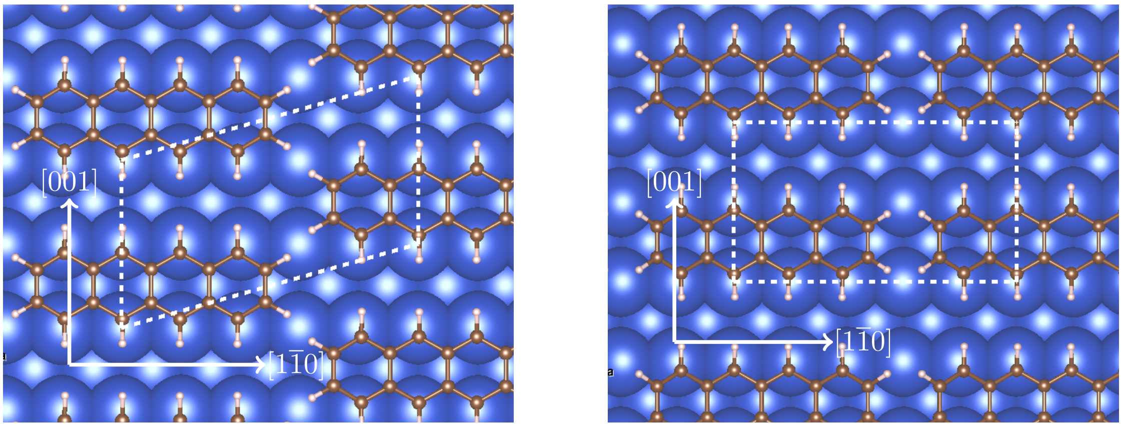

Figure 3.3: Relaxed supercells for the tetracene/Cu(110) interface, *left*: $\boldsymbol{A}_1$, *right*: $\boldsymbol{A}_2$

For each adsorption pattern, we investigated four different adsorption sites, which are named according to the position of the two central tetracene rings with respect to the surface atoms (see Fig. 3.4).

From the comparison in Table 3.3 we can see, that for the hollow, long bridge and top adsorption sites, the chess board pattern is slightly more favorable. Among the adsorption sites the top and short bridge sites are clearly unfavored, while the hollow and long bridge sites yield comparable energies with a slight preference for the latter. All in all the chess board pattern with the long bridge adsorption site is the energetically most favorable geometry.

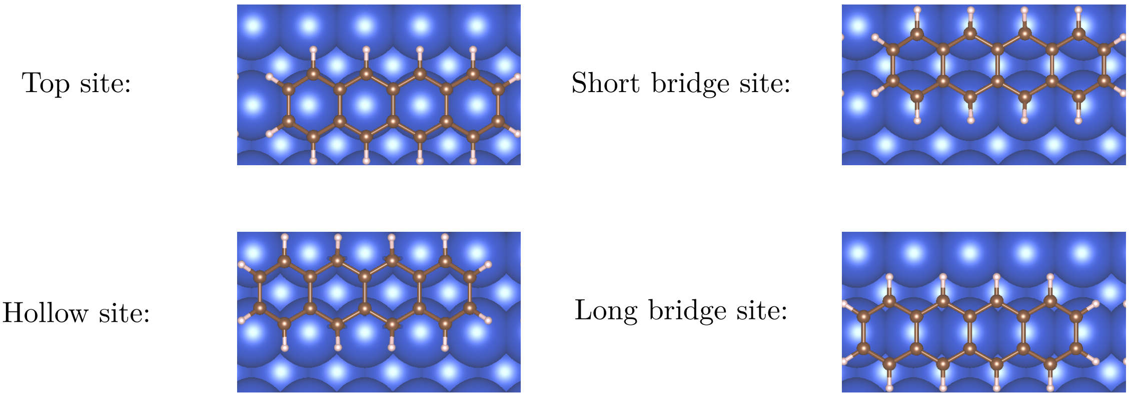

Top site: Short bridge site:

Hollow site: Long bridge site:

Figure 3.4: Different adsorption sites of tetracene on the Cu(110) surface

Taking a closer look at the side view of a relaxed square and chess board pattern super cell (both in long bridge site) in Fig. 3.5 it becomes apparent why the latter is more favorable: Due to the different geometry the tetracene molecules come closer in the square pattern and thus have to bend much more to adsorb than in the chess board pattern.

From now on we will concentrate on the two most favorable adsorption geometries ($\boldsymbol{A}_1$ in the long bridge adsorption site and $\boldsymbol{A}_2$ also in the long bridge adsorption site) for further analysis. The adsorption heights taken as an average over all heights of atoms belonging to the tetracene molecule are compared in Tab. 3.4. The adsorption height in the $\boldsymbol{A}_1$ geometry is significantly smaller than the height in geometry $\boldsymbol{A}_2$, which is due to the strong deformation of tetracene in the latter case. Note that the shortest carbon-copper distances are comparable for the $\boldsymbol{A}_1$ and $\boldsymbol{A}_2$ structures.

Table 3.3: Comparison of total energies for different supercells of the tetracene/Cu(110) interface

	$\boldsymbol{A}_1$	$\boldsymbol{A}_2$
top site	-407.38 eV	-407.10 eV
hollow site	-408.96 eV	-408.88 eV
long bridge site	-409.02 eV	-408.98 eV
short bridge site	-407.64 eV	-407.67 eV

Table 3.4: Comparison of adsorption height for different supercells of the tetracene/Cu(110) interface

	$\boldsymbol{A}_1$	$\boldsymbol{A}_2$
adsorption height	2.33 Å	2.54 Å

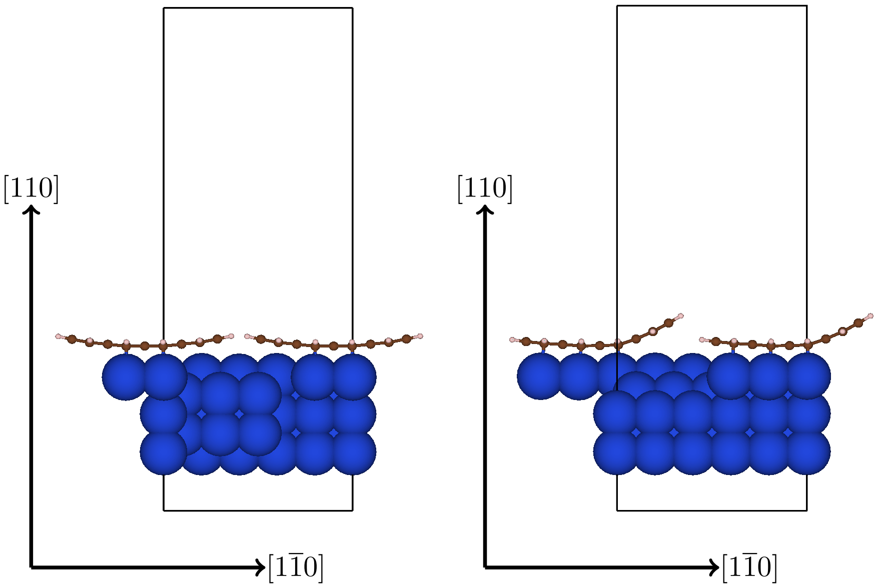

Figure 3.5: Side view of two relaxed supercells for the tetracene/Cu(110) interface, *left*: $\boldsymbol{A}_1$ in long bridge site, *right*: $\boldsymbol{A}_2$ in long bridge site

3.2 Density of States

In this section we compute the density of states (DOS) for both systems and compare the results to photoemission spectroscopy data experiment conducted by Xiaosheng Yang and co-workers from the Peter Grünberg Institute (PGI-3) at the Forschungszentrum Jülich [27].

The DOS is a quantity of great interest because it carries information about the electronic structure of a system: The peaks in the DOS indicate the locations of molecule orbitals.

In this work two methods are used to obtain the DOS from the output data produced by a VASP calculation:

- **projected density of states (pDOS)** The pDOS can be extracted from the *PROCAR* file, which contains the band energy for each k-point split up into contributions from each atomic orbital.

- **molecular orbital projected density of states (mopDOS)** To calculate the mopDOS a separate VASP calculation for the free standing molecule has to be carried out. Then the Kohn-Sham wave functions, which can be obtained from the *WAVECAR* file from the full system and the free standing molecule are used to perform a projection of the DOS on the molecule orbital of the freestanding molecule layer. [28]

Experimentally, the information is contained by so-called energy distribution curve (EDC). The EDC is measured using photoemission spectroscopy, which was briefly introduced in 2.4.1.

3.2.1 The Tetracene/Ag(110) Interface

In Fig. 3.6 the pDOS of both orientations of tetracene on silver are compared to an experimental EDC. It is important to note, that the presented pDOS is a DOS projected on the molecular orbitals of tetracene and therefore represents the proportion of the DOS of the tetracene/Ag(110) system, which is related to the tetracene molecule. The EDC on the other hand represents the whole tetracene/Ag(110) system. It should also be noted that the experimental data can only yield the occupied DOS showing a characteristic Fermi edge around the Fermi energy, while in the computed DOS we do not include a Fermi-Dirac distribution, which is why in this case also the unoccupied DOS is shown.

The pDOS of the parallel and perpendicular orientation are rather similar, both show the lowest unoccupied molecular orbital (LUMO - denoted as L in Fig. 3.6) slightly above the Fermi edge and partially occupied upon adsorption of tetracene on silver. The the highest occupied molecular orbital (HOMO - denoted as H) is approximately at the same energy and the third peak is actually a double peak for both orientations - note the shoulder at the right slope! We name those two peaks HOMO-1 and HOMO-2 (H-1 and H-2 in the picture).

The EDC also shows four peaks in total. The first peak (M1 in the picture) can be identified with the left slope of the LUMO. The fact, that the LUMO appears in the experimental data at all confirms its partial occupation, since only occupied orbitals can be detected using photoemission spectroscopy.

Moreover the experimental peak M2 can be matched to the HOMO peak from the pDOS, but for M3 and M4 an assignment is not at all clear at this point.

In Table 3.5 the peak positions from Fig. 3.6 as well as the respective HOMO-LUMO gap are listed for comparison.

Looking at the comparison of pDOS and mopDOS Fig. 3.7 the nature of the double peak (H-1 and H-2) becomes apparent: It consists of two peaks from separate molecular orbitals (H-1 and H-2).

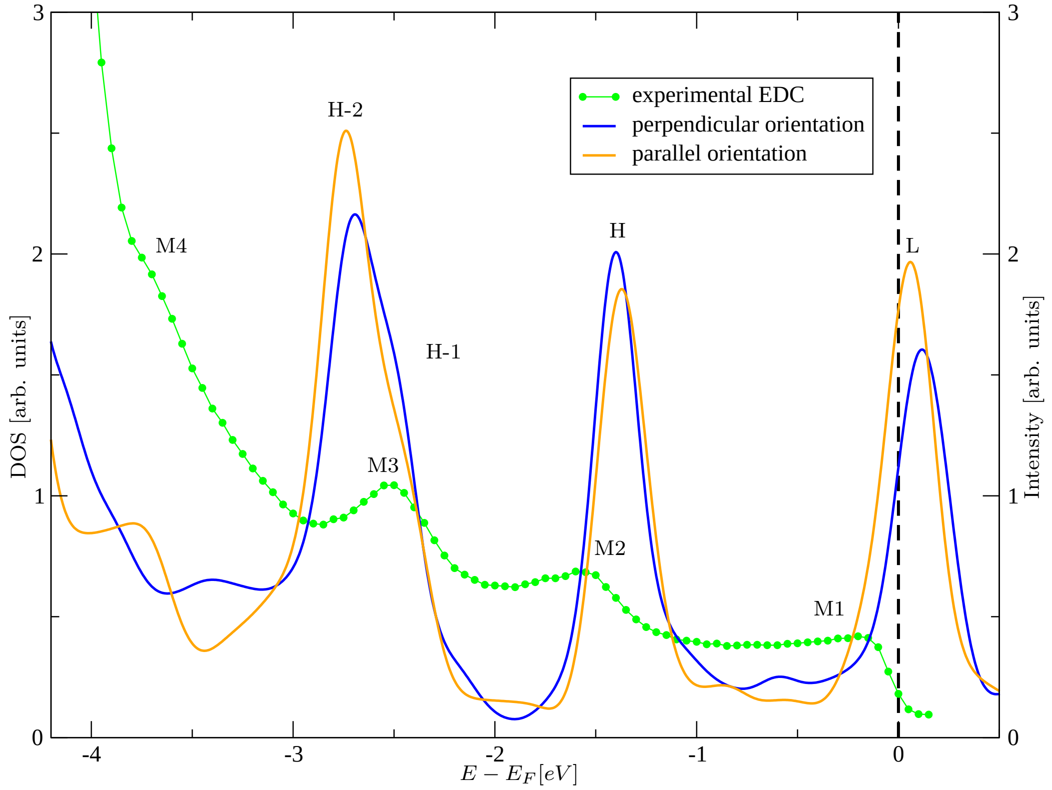

Figure 3.6: pDOS of the $\boldsymbol{A}_{\parallel}$ and the $\boldsymbol{A}_{\perp}$ tetracene/Ag(110) interface in comparison with the EDC from experiment [27]

Table 3.5: Presumed molecular orbital positions from calculated pDOS and experimental EDC for the tetracene/Ag(110) system

	L	H	H-1	H-2	H-L gap
pDOS: $\boldsymbol{A}_{\parallel}$ calculation	0.08 eV	-1.36 eV	-2.46 eV	-2.73 eV	1.44 eV
pDOS: $\boldsymbol{A}_{\perp}$ calculation	0.13 eV	-1.39 eV	-2.47 eV	-2.69 eV	1.52 eV
	M1	M2	M3	M4	M2-M1 gap
experimental [27]	-0.15 eV	-1.55 eV	-2.45 eV	-3.20 eV	1.40 eV

3.2.2 The Tetracene/Cu(110) Interface

In Fig. 3.8 the pDOS for the $\boldsymbol{A}_2$ and $\boldsymbol{A}_2$ geometry are shown together with the experimental EDC of the tetracene/Cu(110) system. Both pDOS curves show two peaks associated with the tetracene molecule (L and H) before the copper d-bands begin. We interpret this peaks as HOMO and LUMO. The LUMO appears slightly below the Fermi edge, hence is occupied upon adsorption of tetracene on copper.

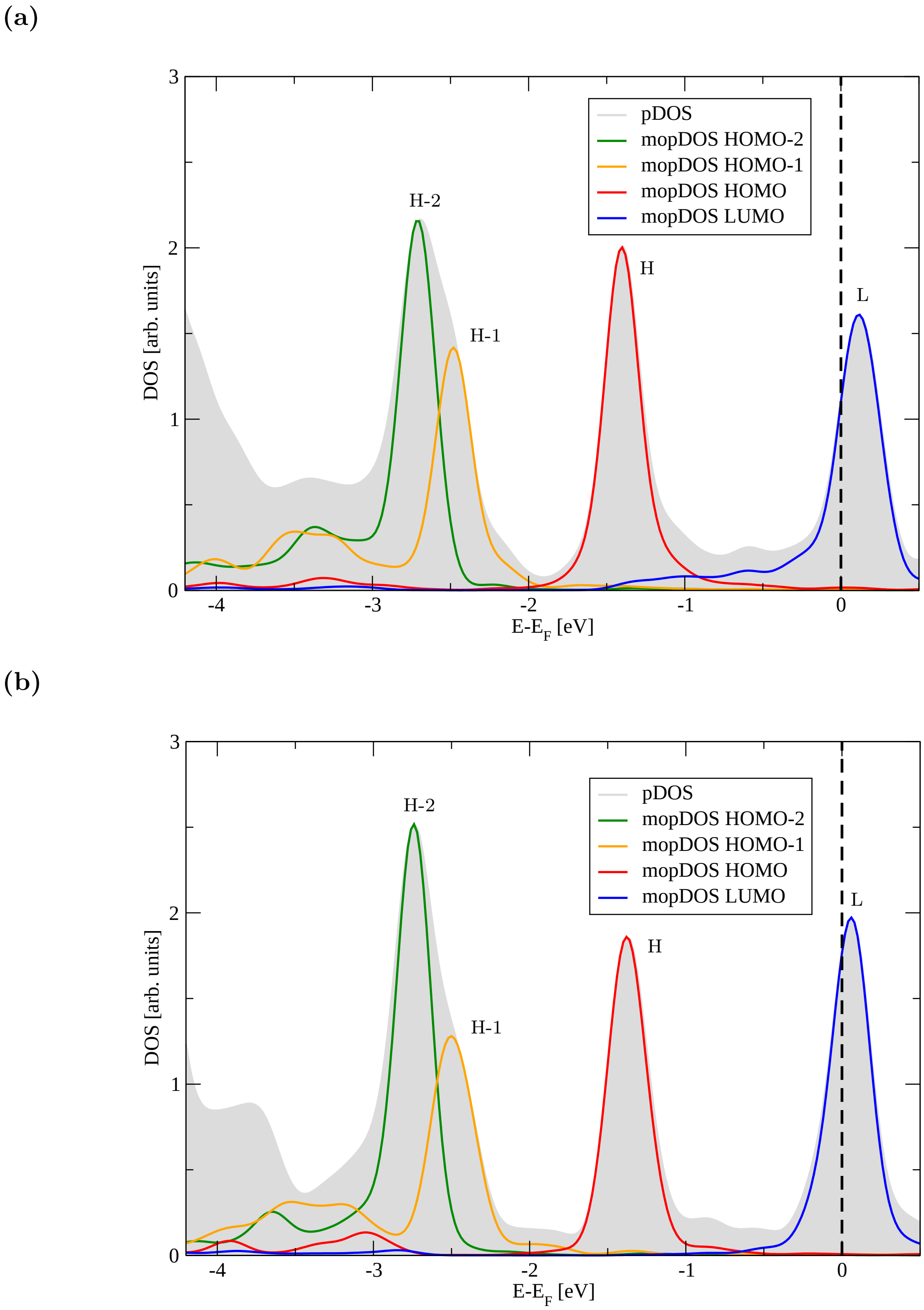

Figure 3.7: Comparison of mopDOS and pDOS for (a) $\boldsymbol{A}_{\perp}$ and (b) $\boldsymbol{A}_{\parallel}$ adsorption geometry for the tetracene/Ag(110) system

The experimental EDC also shows two peaks (M1 and M2), but both appear at a higher binding energy than the calculated peaks. This can also be seen from the comparison of peak positions in Tab. 3.6. Moreover HOMO-LUMO gaps are compared: They are larger for both geometries of tetracene on Cu(110) than the experimental result, whereby the energetically more favorable geometry $\boldsymbol{A}_1$ yields a satisfyingly good estimate of the HOMO-LUMO gap.

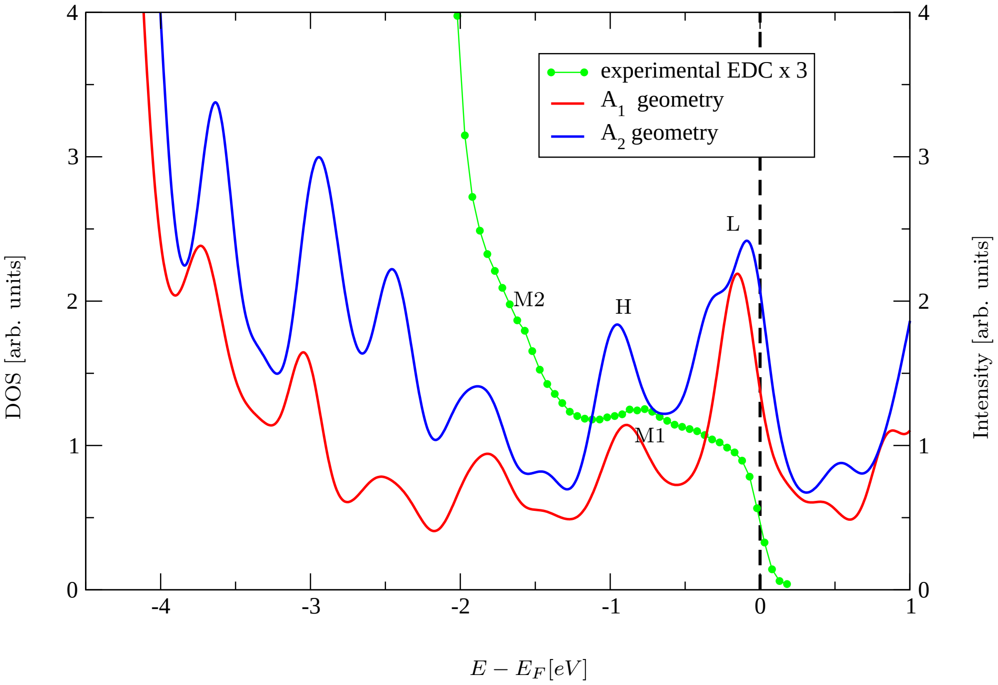

Figure 3.8: Comparison of mopDOS, pDOS and experimental EDC [27] for the tetracene/Cu(110) system

Table 3.6: Presumed molecular orbital positions from calculated pDOS and experimental EDC for the tetracene/Cu(110) system

	L	H	H-L gap
pDOS: $\boldsymbol{A}_1$ calculation	-0.14 eV	-0.89 eV	0.75 eV
pDOS: $\boldsymbol{A}_2$ calculation	-0.08 eV	-0.95 eV	0.87 eV
	M1	M2	M1-M2 gap
experimental	-0.82 eV	-1.52 eV	0.70eV

A comparison of the calculated pDOS to the calculated mopDOS can be seen in Fig. 3.9. The mopDOS curves confirm the previous assignment of peaks. Note that the LUMO peak in 3.9 (b) has a double peak structure with a shoulder on its left slope for the $\boldsymbol{A}_2$ structure, which may be due to the pronounced bend of the molecule or arise from strong intermolecular dispersion. However in contrast to the H-1 H-2 double peak from tetracene/Ag(110) (Fig. 3.6) it only describes one orbital as shown by the mopDOS calculation.

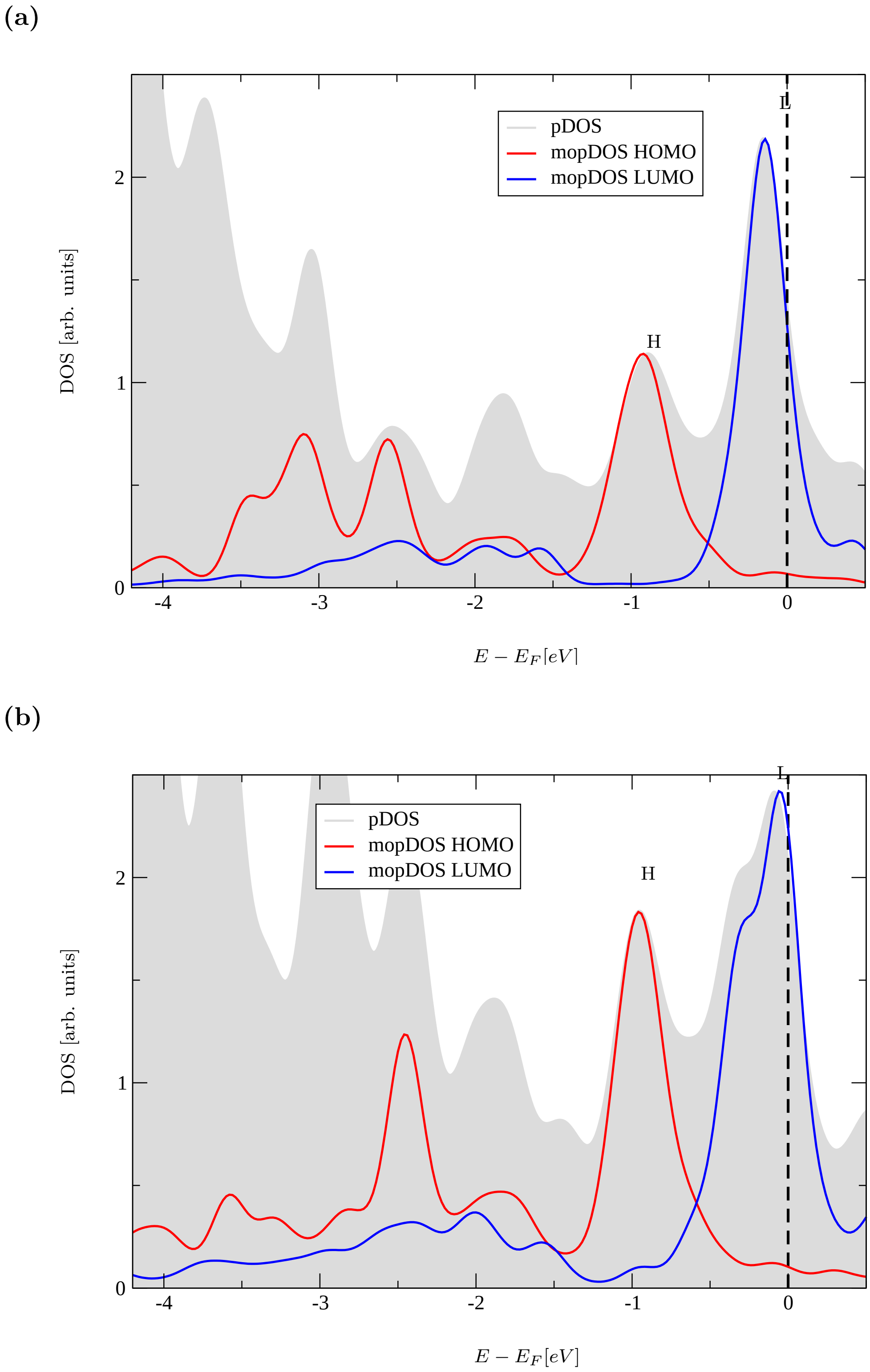

Figure 3.9: Comparison of mopDOS to pDOS for the tetracene/Cu(110) system in (a) the $\boldsymbol{A}_1$ geometry and (b) the $\boldsymbol{A}_2$ geometry

3.3 Charge Rearrangements and Work Function Variations

In this section we look at the charge density of both interfaces and compare them to the charge density of the bare surface. We will observe charge rearrangements and moreover discuss the closely related work function variations. The work function is the energy needed to remove an electron from the system to the vacuum level and therefore a quantity of great interest especially concerning technical applications. The work function is influenced by the surface dipole layer, which exists at a bare surface because of the spilling of the electrons outside the ionic lattice of the solid. Those spilled electrons create an excess of negative charge above the surface and a positively charged area right beneath the surface. The resulting dipole layer acts as a barrier when extracting an electron from the system and therefore increases the work function. When a layer of molecules adsorbs on a surface the dipole layer is altered hence the work function of the system changes. This is mostly caused by two effects:

- Due to Pauli's principle the adsorbed molecules push the spilled out electrons, which are causing the surface dipole layer, a bit back into the solid as pictured in 3.10. This is called the **push back effect** and it results in a lowering of the work function.
- The second effect is **charge transfer** from the solid to the adsorbed molecule, which has the opposite impact on the work function of the system, namely an increased work function.

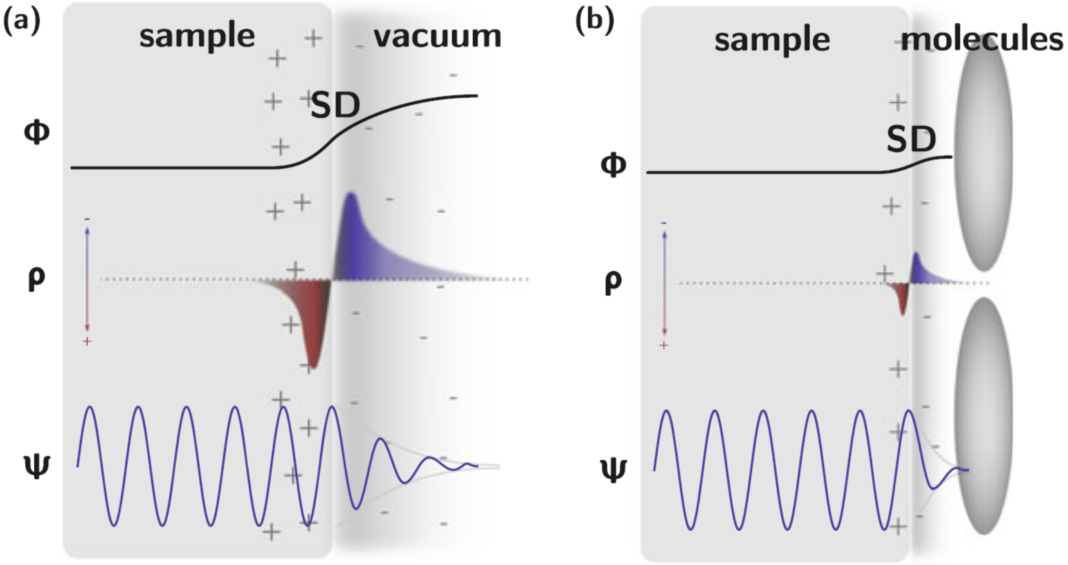

Figure 3.10: Schematic representation of the push back effect from [29]

The work function modification $\Delta\Phi$ can be gained from a charge density analysis, as described in [30]:

1. Calculate the difference in charge density $\Delta\rho$ regarding the combined system versus the bare surface.

2. Solve the one-dimensional Poisson's equation for the plane-averaged charge density difference, thus integrate $\Delta\rho$ twice over space to obtain the electrostatic potential associated with $\Delta\rho$.
3. The jump in the calculated potential equals the work function variation $\Delta\rho$ (see Figs. 3.11 and 3.12).

As a second possibility, the work function variation $\Delta\Phi$ can be evaluated directly from the respective electrostatic potential values:

$$\Delta\Phi = \Phi(\mathrm{surf/mol}) - \Phi(\mathrm{surf}) \tag{3.9}$$

where Φ(surf/mol) is the work function of the combined system and Φ(surf) is the work function of the surface by its own.

The work function is

$$\Phi = E_{\mathrm{vac}} - E_F \tag{3.10}$$

where E_{vac} is the vacuum energy and E_F is the Fermi energy. This can be computed from a VASP calculation: E_{vac} can be identified from the electrostatic potential, which is contained by the VASP output file *LOCPOT* and E_F can be found in the *OUTCAR* file.

3.3.1 The Tetracene/Ag(110) Interface

In Fig. 3.11 we see the charge density analysis for tetracene on silver in a perpendicular and a parallel adsorption orientation. Comparing both we see almost no difference, with the exception of the total charge density of the surface, which is higher in 3.11 (b) due to the higher number of silver atoms in the respective super cell. In both cases $\Delta\rho$, the charge density variation, and the 'potential' ($\Delta\rho$ integrated two times over space) were scaled by a factor of 100. Looking at $\Delta\rho$ (blue curve) we see a series of bonding dipoles, which are a consequence of the push back effect and a slight charge transfer from the silver surface to the tetracene molecule layer.

Measuring the potential jump to get the work function variation $\Delta\Phi$, we get -0.40 eV for the perpendicular adsorption orientation and -0.36 eV for the parallel adsorption orientation, while we get -0.42 eV and -0.43 eV respectively from the direct calculation. In Table 3.7 we see a comparison of both methods to compute the work function variation.

The results are in relatively good agreement and state consistently, that the work function is lowered upon adsorption of tetracene on silver. For the sake of completeness the additional dipole due to the geometric distortion of the tetracene molecules is an is shown in Table 3.7. In [31] this effect is called bend dipole as opposed to the bond dipole arising from charge rearrangements. Since this geometric distortion of tetracene on silver is rather small the bend diplole does not play an important role. For the case of tetracene on copper on the other hand it has a crucial influence on the work funktion as will be discussed in the next section.

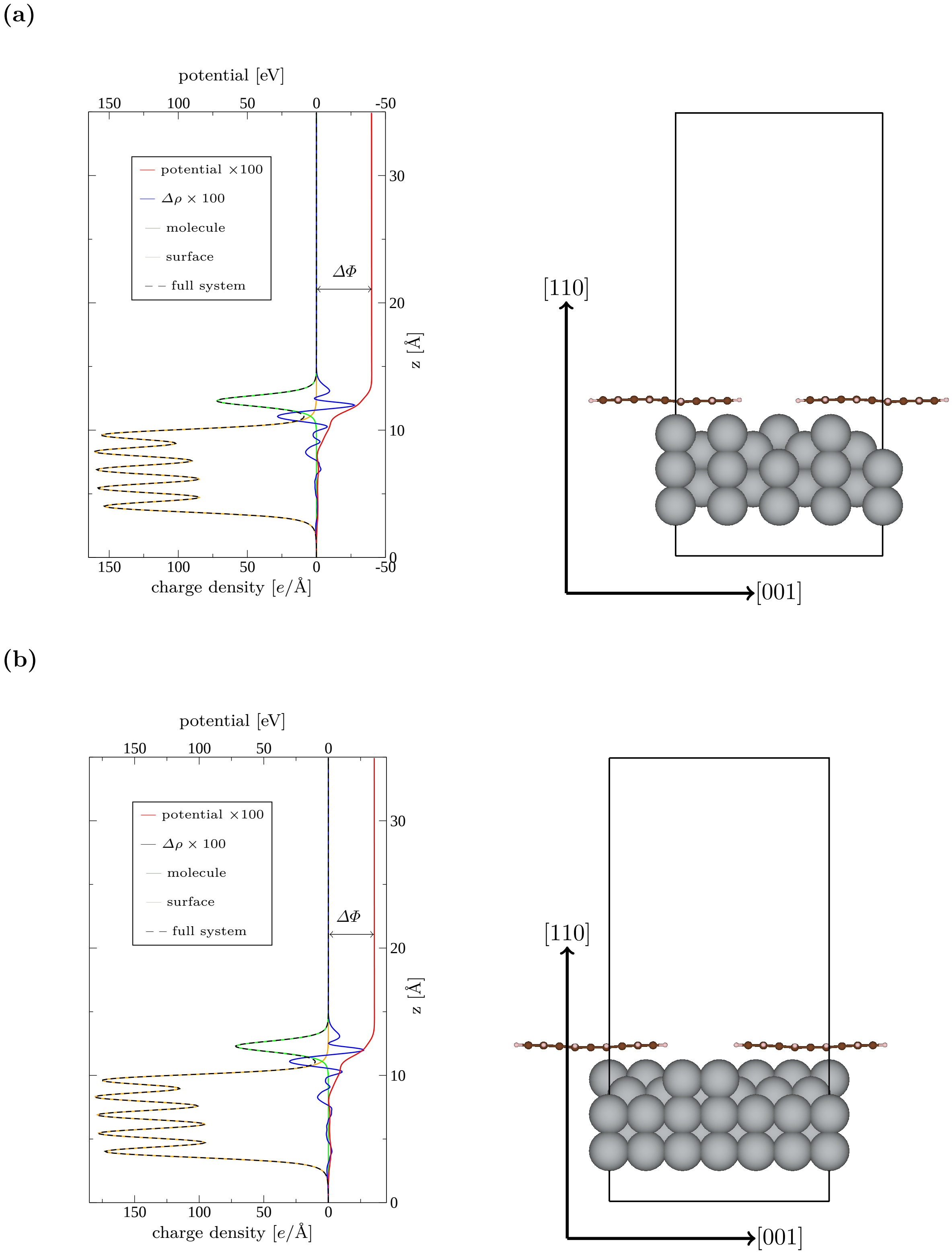

Figure 3.11: Charge density analysis for (a) the $\boldsymbol{A}_{\perp}$ and (b) the $\boldsymbol{A}_{\parallel}$ tetracene/Ag(110) interface

Table 3.7: Work function variation of the tetracene/Ag(110) system

	$\boldsymbol{A}_\perp$	$\boldsymbol{A}_\parallel$
$\Delta\Phi$ from Eq. 3.9	-0.40 eV	-0.36 eV
bond dipole	-0.42 eV	-0.43 eV
bend dipole	-0.01 eV	-0.07 eV

3.3.2 The Tetracene/Cu(110) Interface

The charge rearrangement analysis for tetracene on copper is shown in Fig. 3.12. We see a overall similar result compared to the tetracene/Ag(110) system:

The charge density variation $\Delta\rho$ shows strong oscillations in the region between molecule and surface indicating a series of bonding dipoles caused by the push back effect. In fact the present oscillations have a higher amplitude than the ones observed for the tetracene/Ag(110) system. This possibly is the direct result of a stronger push back effect due to a smaller adsorption height. Despite those strong bonding dipoles the work function variation $\Delta\Phi$ seen from the change in the electrostatic potential associated with $\Delta\rho$ is not considerably larger than the ones seen concerning the tetracene/Ag(110) system for neither of both present adsorption geometries ($\boldsymbol{A}_1$ and $\boldsymbol{A}_2$). This puzzling fact can be clarified by recalling the position of the LUMO in the calculated density of states (Fig. 3.8), which is beneath the Fermi edge and indicates a strong charge transfer from the copper surface to the tetracene molecules. The charge transfer reverses part of the the effect caused by bonding dipoles, but the push back effect still dominates thus in total Φ is lowered upon adsorption of tetracene on copper.

In Tab. 3.8 a comparison of both discussed methods to gain the work function variation $\Delta\Phi$ from a DFT calculation is shown. The values measured from charge density analysis are considerably lower than the values calculated according to 3.9, but consistently state a lowering of the work function. The difference between the two methods arises from an additional dipole due to the geometric distortion of the tetracene molecules, which is not taken into account in the charge rearrangement analysis. The upward bending of the H-atoms introduces the bend dipole, which can be seen from Tab. 3.8. In this case, the bend dipole acts as a barrier for the spilled electrons and therefore lowers the work function.

Table 3.8: Work function variation of the tetracene/Ag(110) system

	$\boldsymbol{A}_1$	$\boldsymbol{A}_2$
$\Delta\Phi$ from Eq. 3.9	-0.52 eV	-0.53 eV
bond dipole from charge density analysis	-0.21 eV	-0.11 eV
bend dipole	-0.42 eV	-0.50 eV

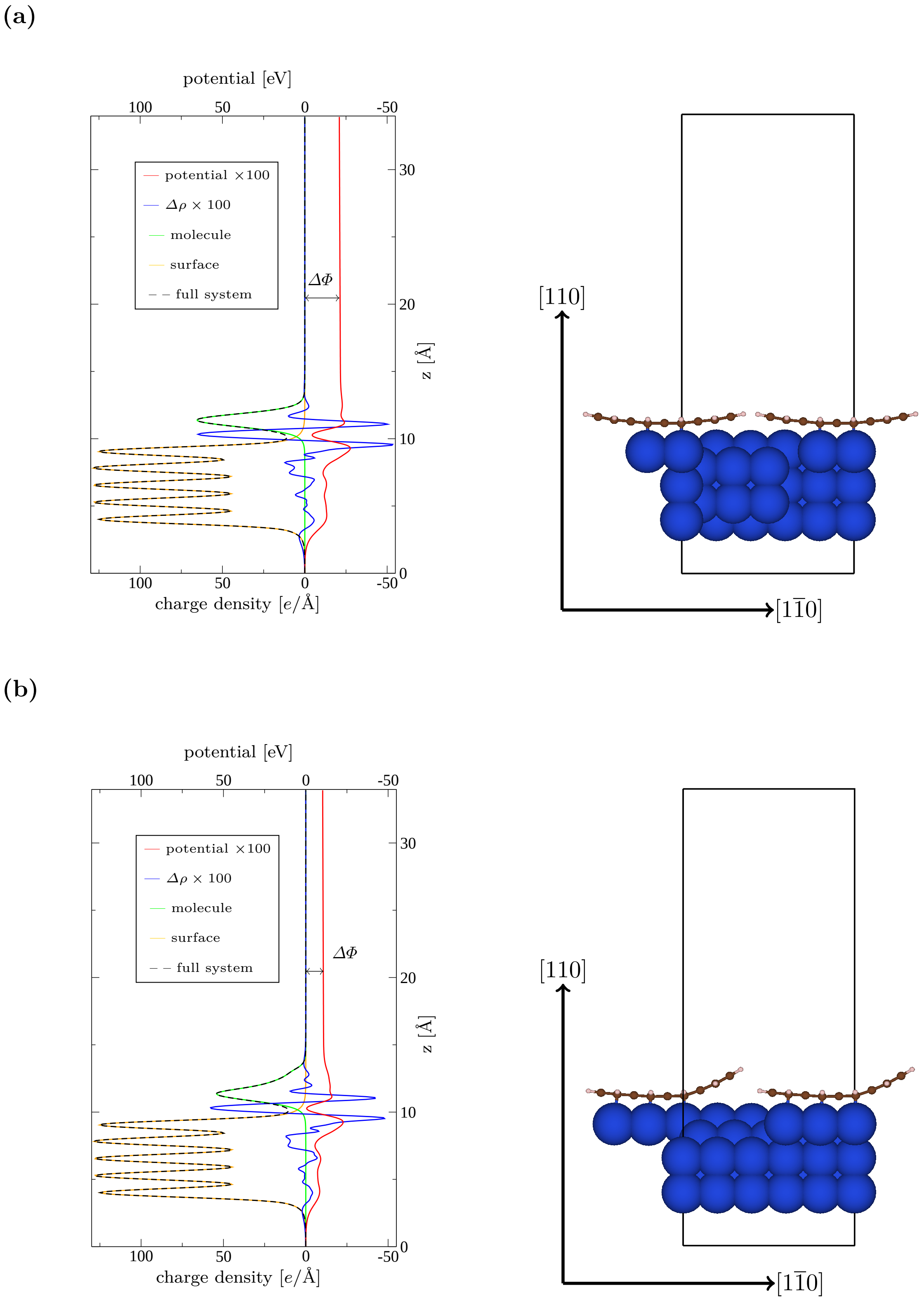

Figure 3.12: Charge density analysis for (a) the $\boldsymbol{A}_1$ and (b) the $\boldsymbol{A}_2$ tetracene/Cu(110) interface

3.4 Photoemission Momentum Maps

In this section the method discussed in 2.4.2 is used to simulate photoemission momentum maps for both interfaces and subsequently the simulated maps are compared to experimental data measured by Xiaosheng Yang and co-workers from the Peter Grünberg Institute (PGI-3) at the Forschungszentrum Jülich [27].

3.4.1 The Tetracene/Ag(110) Interface

The photoemission angular distribution measured over wide polar and azimuthal angular ranges can be used as a fingerprint for molecular emissions. Here, we simulate such momentum maps as resulting from angle-resolved photoemission spectroscopy (ARPES). To this end, we have to specify at which energy level we want to image the electronic structure in k-space. For this task we use the peak energies from the calculated DOS given in Table 3.5 to visualize the molecular orbitals of the system.

In Fig. 3.13 we see a comparison of simulated to measured ARPES maps. The first thing, that catches the eye is the alignment of the ARPES maps, which is alike for the simulation of a parallel adsorption pattern and the experimental data, but rotated by an angle of 90 degrees for the simulation of a perpendicular adsorption pattern. This can best be seen for the molecular emission right below the Fermi level, which exhibits pronounced peaks around $k_{\|} \approx 1.5\text{Å}^{-1}$ along the molecular axis. This fact clearly indicates, that the tetracene molecules in the experiment are adsorbed parallel to the close-packed rows. Therefore we can conclude that the $\boldsymbol{A}_{\|}$ structure describes the correct adsorption geometry in agreement with our results for the adsorption energy presented earlier in 3.1.

The first experimental orbital (M1) exhibits a comparably weak intensity and takes a form in k-space similar to the simulated LUMO. The observation of a peak that can be identified with the LUMO confirms the finding from previous analysis, namely that the LUMO gets partially occupied upon adsorption of tetracene on silver. M2 resembles the simulated HOMO ARPES map, but so does M3. Judging from the M3 energy, its ARPES map should resemble the HOMO-1 ARPES map, which shows features, that lie much more closely together in k-space than the HOMO features. The last ARPES map (M4) roughly resembles the HOMO-2 map, but could also be interpreted as a superposition of the HOMO-2 and the HOMO-1 map.

A feasible hypothesis explaining these observations is the existence of a second layer of tetracene in the experiment, which may be responsible for the somewhat strange second HOMO lookalike peak M3.

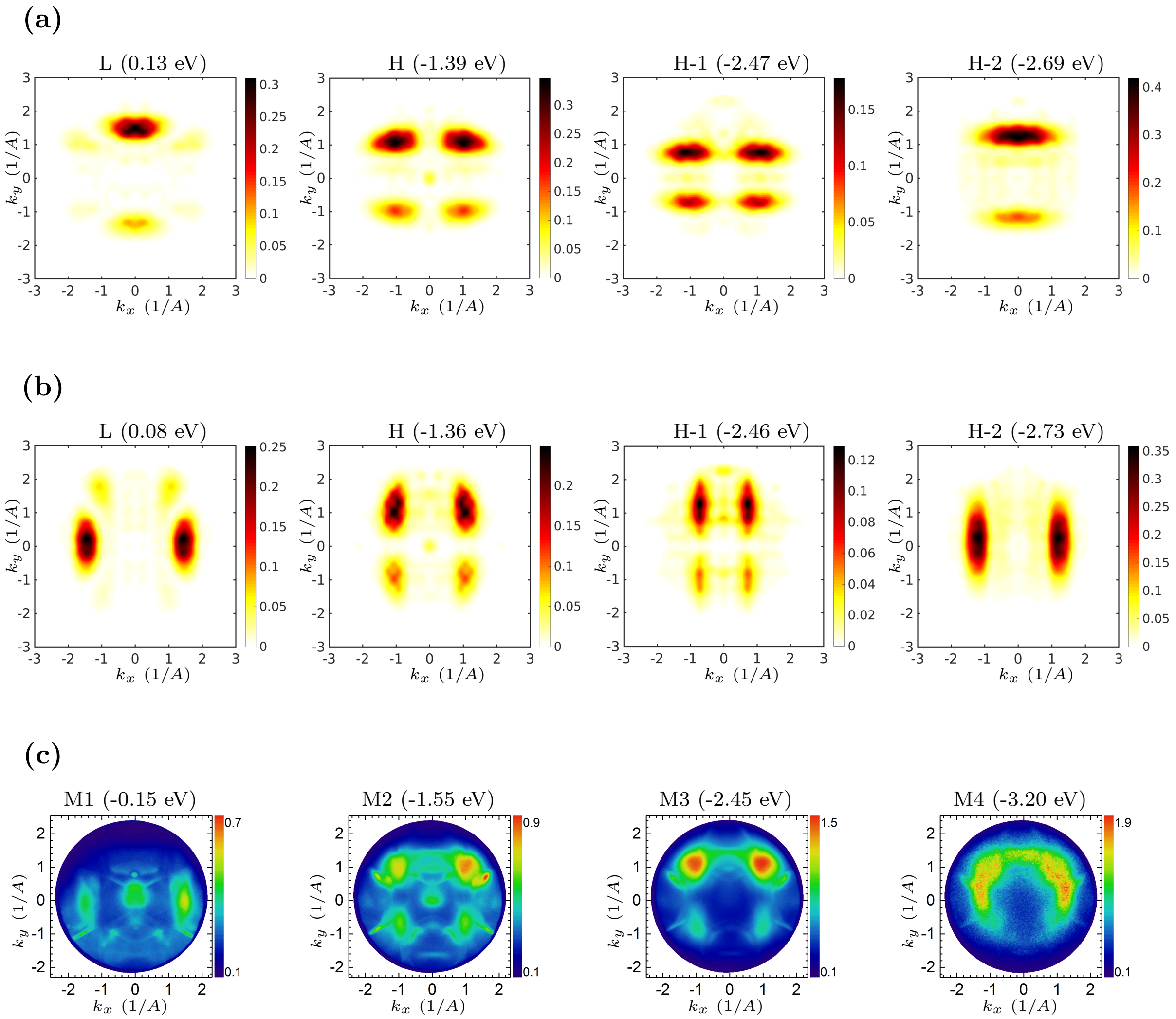

Figure 3.13: **(a)**: simulated ARPES maps for the $\boldsymbol{A}_\perp$ adsorption geometry, **(b)**: simulated ARPES maps for the $\boldsymbol{A}_\parallel$ adsorption geometry, **(c)**: ARPES maps from experimental data [27]

Putting this hypothesis to the test an ionic relaxation calculation for a double layer of tetracene on the Ag(110) surface, with a parallel adsorption orientation regarding the close-packed rows, was conducted. The second layer of tetracene was placed in a chess board like manner on top of the first layer.

Looking at the side view of the relaxed supercells in Fig. 3.14, we see that for a coverage of 0.47 molecules per nm^2 , as in Fig. 3.1 on the right side, during relaxation the tetracene molecules from the second layer twist slightly and dive into the gaps between the tetracene molecules of the first layer resulting in a merging of the second layer with the first layer.

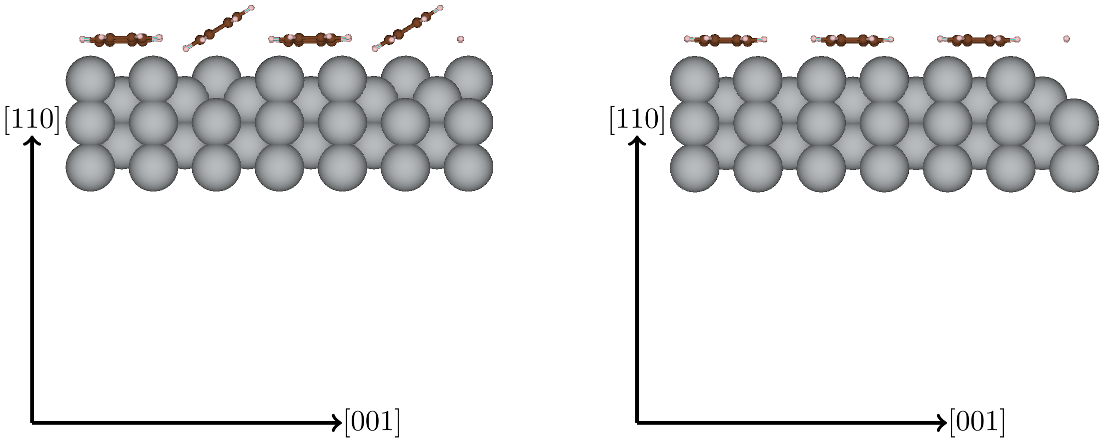

Figure 3.14: Side view of the supercells containing a double layer of tetracene on Ag(110), *left*: super cell from Fig. 3.1 right side with an extra layer of tetracene added, *right*: new super cell with a higher coverage

Consequently we continue the investigation of a double layer of tetracene on Ag(110) with a considerably larger coverage of 0.85 molecules per nm^2 The side view of the relaxed super cell using this higher coverage is shown in Fig. 3.14 on the right side. One sees two separate layers of tetracene on top of each other.

To find the energy positions of the molecular orbitals of this new system we calculate the pDOS, this time projecting on the first and second layer of tetracene separately. The resulting pDOS curves are compared to the experimental EDC in Fig. 3.15. As expected for both layers of tetracene we see a similar pDOS, whereby the pDOS of the upper tetracene layer is shifted towards higher energies. This pattern can also be seen from the energies in Table 3.9, where all peak positions are listed for comparison. To distinguish the peaks from the upper and lower layer of tetracene the subscripts u and l respectively have been introduced.

Moreover one notes that the coverage of tetracene on silver does influence the peak positions in the projected density of states: All peak positions except for the LUMO peak position shift to lower binding energies with a higher coverage. A possible explanation for the different behavior of the LUMO could be a higher charge transfer from silver to the molecule layer at higher coverage, which would lower the position of the LUMO in reference to the Fermi energy.

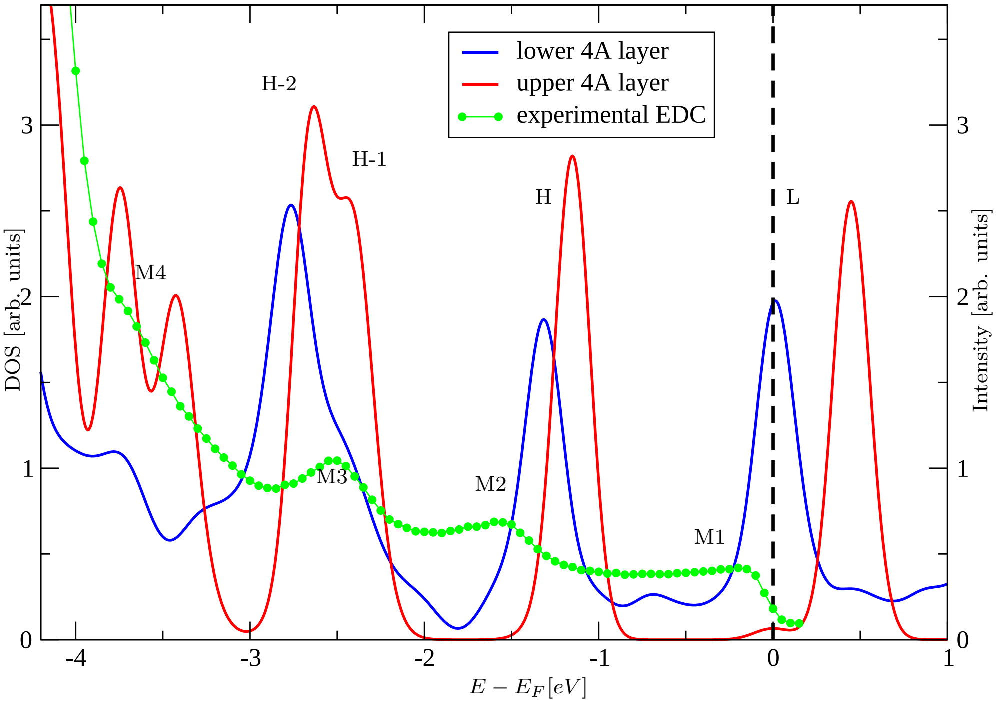

Figure 3.15: Comparison of the pDOS of the tetracene double layer on Ag(110) (Fig. 3.14, right side) and the experimental EDC [27]

Table 3.9: Presumed molecular orbital positions from calculated pDOS for a monolayer and a double layer of tetracene on silver in a parallel adsorption position compared to the experimental EDC [27]

	L	H	H-1	H-2
pDOS: monolayer low coverage	0.08	-1.36	-2.46	-2.73
pDOS: monolayer high coverage	0.03	-1.24	-2.38	-2.68
	L$_u$ L$_l$	H$_u$ H$_l$	H-1$_u$ H-1$_l$	H-2$_u$ H-2$_l$
pDOS: double layer high coverage	0.46 | 0.01	-1.15 | -1.31	-2.44 | -2.47	-2.63 | -2.75
	M1	M2	M3	M4
experimental data [27]	-0.15	-1.55	-2.45	-3.20

Looking at the associated simulated ARPES maps compared to the experimental ones in Fig. 3.16 we note that the double layer of tetracene exhibits two HOMO like peaks (H$_l$ and H$_u$) as expected, but their energies do not quite match up with the energies of the two HOMO lookalike peaks observed in experiment (M2 and M3).

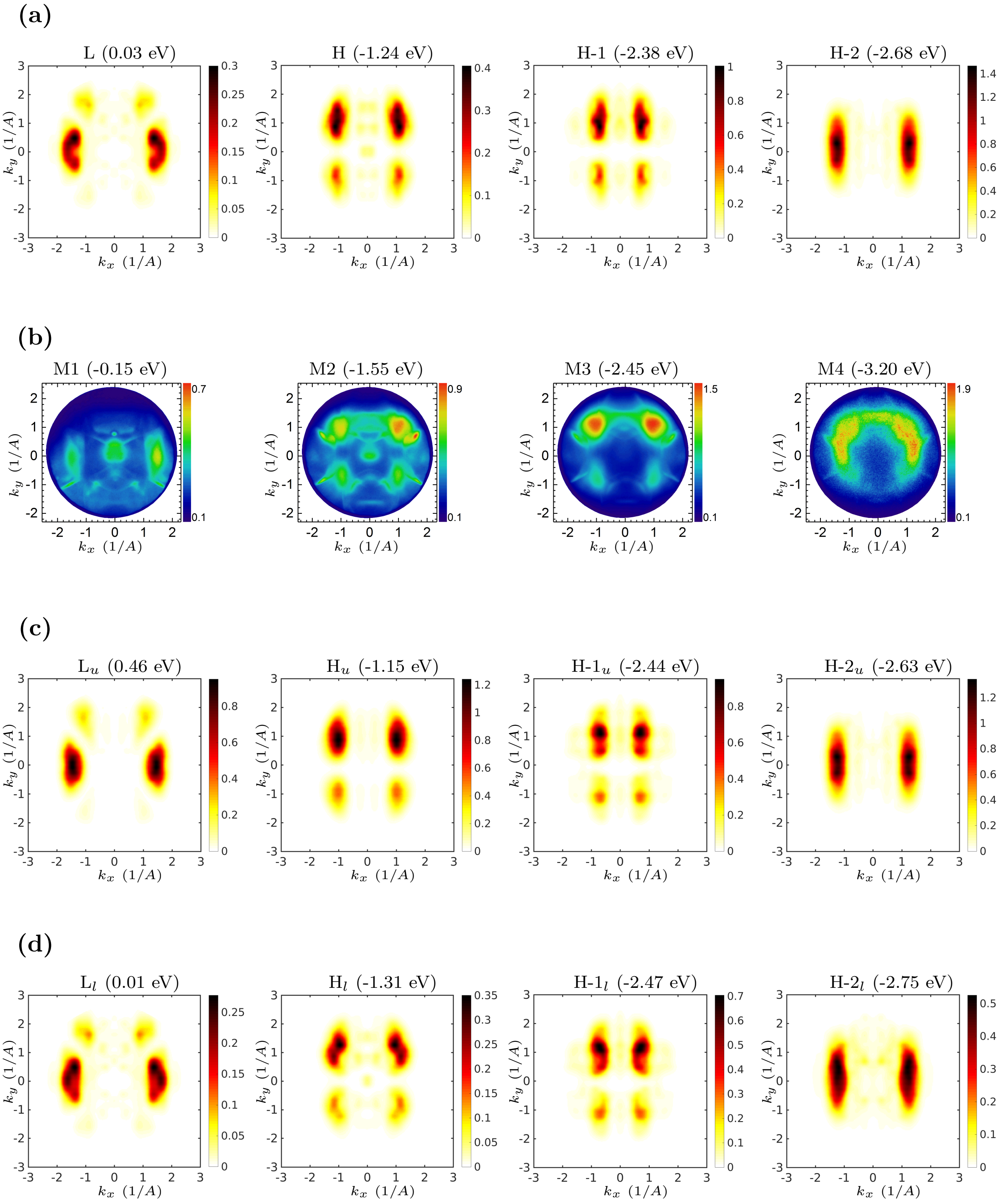

Figure 3.16: **(a)**: simulated ARPES of a monolayer tetracene on silver, **(b)**: ARPES maps from experimental data [27], **(c)**: simulated ARPES of the upper layer of two layers tetracene on silver, **(d)**: simulated ARPES of the lower layer of two layers tetracene on silver

3.4.2 The Tetracene/Cu(110) Interface

In Fig. 3.17 the simulated ARPES maps are compared to maps from photoemission spectroscopy. The orientation of the features seen in all maps is consistent and confirms that tetracene adsorbs parallel to the close-packed rows on a Cu(110) surface.

The simulated LUMO ARPES map can be identified with the experimental M1 map for both tetracene/Cu(110) calculations. The M1 map shows a rather strong intensity, hence shows a filled orbital. This confirms the previously observed charge transfer and occupation of the LUMO upon adsorption of tetracene on Cu(110).

Moreover the HOMO peak can reliably be matched to the experimental M2 peak. The HOMO map shown in Fig. 3.17 (a) ($\boldsymbol{A}_1$ geometry) exhibits the for a tetracene HOMO characteristic features more clearly than the H-map shown in (c) ($\boldsymbol{A}_2$ geometry), which is considerably blurred. This might be a consequence of the strong deformation of tetracene in the $\boldsymbol{A}_2$ geometry. The comparison with the experimental map thus also suggests, that an adsorption geometry with a substantial geometric distortion of tetracene as seen in $\boldsymbol{A}_2$ is rather unlikely.

It should also be noted, that in the simulated maps a substructure is visible, which presumably arises from strong intermolecular dispersion and molekule-substrate interaction. A similar effect was observed and studied in [32] in a coronene/Ag(111) system.

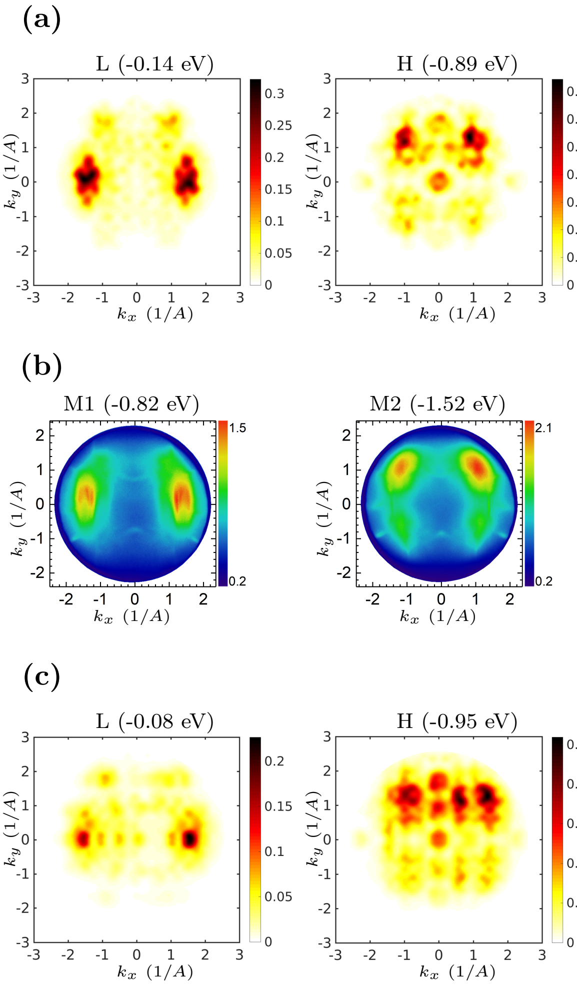

Fig. 3.17: **(a)**: simulated ARPES maps for tetracene on copper in $\boldsymbol{A}_1$ geometry, **(b)**: ARPES maps from experimental data [27],**(c)**: simulated ARPES maps for tetracene on copper in $\boldsymbol{A}_2$ geometry

3.5 Comparison of the Tetracene/Ag(110) Interface to the Tetracene/Cu(110)

In this section we briefly compare the results from both interfaces starting with a comparison of adsorption energies in Tab. 3.10. We see that generally the adsorption energies on Cu(110) are higher than the energies on Ag(110). In particular it is the tetracene/Cu(110) $\boldsymbol{A}_1$ geometry that yields the largest value.

Table 3.10: Comparison of adsorption energies for tetracene on Ag(110) and Cu(110)

	E_{ad}
Tetracene/Ag(110): $\boldsymbol{A}_{\|\|}$	2.12 eV
Tetracene/Ag(110): $\boldsymbol{A}_{\perp}$	2.04 eV
Tetracene/Cu(110): $\boldsymbol{A}_1$	3.32 eV
Tetracene/Cu(110): $\boldsymbol{A}_2$	2.89 eV

Furthermore it also is the tetracene/Cu(110) $\boldsymbol{A}_1$ geometry which exhibits the lowest adsorption height as it can be seen from Tab. 3.11.

Table 3.11: Comparison of adsorption height for tetracene on Ag(110) and Cu(110)

	adsorption height
Tetracene/Ag(110): $\boldsymbol{A}_{\|\|}$	2.51 Å
Tetracene/Ag(110): $\boldsymbol{A}_{\perp}$	2.52 Å
Tetracene/Cu(110): $\boldsymbol{A}_1$	2.33 Å
Tetracene/Cu(110): $\boldsymbol{A}_2$	2.54 Å

From Tab. 3.12 we can consistently state, that tetracene lowers the work function upon adsorption on a Ag(110) surface as well ws an a Cu(110) surface. Moreover both systems exhibit charge transfer from the surface to the tetracene molecule layer. The tetracene/Ag(110) LUMO gets partially occupied but remains slightly above the Fermi edge while the tetracene/Cu(110) LUMO on the other hand is completely occupied upon adsorption and consequently has an energy beneath the Fermi energy.

Table 3.12: Comparison of work function variation for tetracene on Ag(110) and Cu(110)

	direct calculation	bond dipole	bend dipole
Tetracene/Ag(110): $\boldsymbol{A}_{\|\|}$	-0.43 eV	-0.36 eV	-0.07 eV
Tetracene/Ag(110): $\boldsymbol{A}_{\perp}$	-0.42 eV	-0.40 eV	-0.01 eV
Tetracene/Cu(110): $\boldsymbol{A}_1$	-0.52 eV	-0.21 eV	-0.42 eV
Tetracene/Cu(110): $\boldsymbol{A}_2$	-0.53 eV	-0.11 eV	-0.50 eV

Finally we compare HOMO-LUMO gaps for both systems. From Tab. 3.13 we see, that the present calculations throughout yield slightly larger gaps than the experiment does. Interestingly the systems that were slightly favorable regarding adsorption engergy ($\boldsymbol{A}_{||}$ for Ag(110) and $\boldsymbol{A}_1$ for Cu(110)) also give the best results concerning the HOMO-LUMO gap.

Table 3.13: Comparison of the HOMO-LUMO gap for tetracene on Ag(110) and Cu(110)

	HOMO-LUMO gap
Tetracene/Ag(110): $\boldsymbol{A}_{\parallel}$	1.44 eV
Tetracene/Ag(110): $\boldsymbol{A}_{\perp}$	1.52 eV
Tetracene/Ag(110): experiment [27]	1.40 eV
Tetracene/Cu(110): $\boldsymbol{A}_1$	0.75 eV
Tetracene/Cu(110): $\boldsymbol{A}_2$	0.87 eV
Tetracene/Cu(110): experiment [27]	0.70 eV

CHAPTER 4

Conclusion

The goal of this thesis was to gather detailed knowledge about the electronic properties of the tetracene/Ag(110) and the tetracene/Cu(110) interface. Moreover we aimed to better understand and interpret data from experimental research by comparison to theoretical simulations.

This challenge was tackled by means of density functional theory calculations which were carried out using VASP. The first step was to investigate the optimal adsorption geometry as a basis for further analysis.

For the tetracene/Ag(110) interface we choose two geometries, namely parallel ($\boldsymbol{A}_{\parallel}$) and perpendicular ($\boldsymbol{A}_{\perp}$) to the close-packed rows. They were studied in terms of adsorption energy and adsorption height. Contradictory to literature [24] the present calculations suggest that the adsorption geometry parallel to the close-packed Ag(110) rows is energetically preferred over the perpendicular alignement by 80 meV.

To find the optimal adsorption geometry for the tetracene/Cu(110) system, we examined two strucures proposed by literature [25, 26], which both have the same coverage, but a different arrangement of the tetracene molecules: In the $\boldsymbol{A}_1$ structure the molecules are arranged in a chess board pattern, whereas in the $\boldsymbol{A}_2$ structure they are arranged face-to-face. Moreover we analyzed all four high-symmetry adsorption sites for both structures respectively. We found, that the long bridge adsorption site is clearly preferred in both structures of tetracene on copper, while the $\boldsymbol{A}_1$ structure is slightly more favorable energetically than the $\boldsymbol{A}_2$ structure.

As a next step we computed the density of states and found that the LUMO gets partially occupied upon adsorption of tetracene on Ag(110). This effect proved to be even stronger for the case of tetracene/Cu(110), where one finds a filled LUMO beneath the Fermi edge. A comparison of the simulated DOS to the experimental photoemission data showed a satisfyingly good agreement of the HOMO-LUMO gaps calculated from the tetracene/Ag(110) $\boldsymbol{A}_{\parallel}$ and the tetracene/Cu(110) $\boldsymbol{A}_1$ structure to experimental data while both other structures yielded HOMO-LUMO gaps considerably larger than the experimental gaps.

A charge rearrangement analysis showed charge transfer from the surface to the tetracene layer accompanied by the formation of bonding dipoles due to the push back effect in both systems. However the push back effect outweighs the effect of charge transfer, which results in a lowering of the work function upon adsorption of tetracene on Ag(110) as well as on Cu(110).

Finally we simulated ARPES maps and compared them to experimental ARPES maps.

The analysis of the tetracene/Cu(110) system showed consistent results clearly confirming the adsorption of tetracene parallel to the close-packed Cu(110) rows as well as the filling of the LUMO. The simulated ARPES maps concerning the tetracene/Ag(110) system likewise confirm the partial occupation of the LUMO as well as adsorption of tetracene parallel to the close-packed Ag(110) rows. However the simulated ARPES maps show LUMO, HOMO, HOMO-1 and HOMO-2 patterns as expected while in the experimental data shows two HOMO lookalike maps. Presuming a second layer of tetracene could be the cause of the second HOMO peak, a DFT calculation using a double layer of tetracene on Ag(110) was performed. From this calculation we obtain a second HOMO peak but not at the same energy as in the experiment. This subject remains an open question, future work will be necessary to clarify this issue.

Acknowledgments

I would like to express my very great appreciation to my thesis supervisor Professor Peter Puschnig for the sincere and valuable guidance, his professional advise and for always having an open ear for all my questions.

I would also like to offer my special thanks to my colleagues, friends and family for their support.

CHAPTER 5

Bibliography

1. Czycholl, Gerd: *Theoretische Festkörperphysik: Von den klassischen Modellen zu modernen Forschungsthemen.* Springer Verlag, 2008 (cit. on p. 3).
2. Perdew, J. P. and S. Kurth: *A Primer in Density Functional Theory.* Ed. by Fiolhais, C., F. Nogueira, and M. A. L. Marques. Springer, Berlin, 2003 (cit. on p. 4).
3. Levy, Mel: 'Universal variational functionals of electron densities, first-order density matrices, and natural spin-orbitals and solution of the v-representability problem'. *Proc. Natl. Acad. Sci. USA* (1979), vol. 76: p. 6062 (cit. on p. 4).
4. Hohenberg, P. and W. Kohn: 'Inhomogeneous Electron Gas'. *Phys. Rev.* (1964), vol. 136: B864 (cit. on pp. 4, 5).
5. Kohn, W. and L. J. Sham: 'Self-Consistent Equations Including Exchange and Correlation Effects'. *Phys. Rev.* (1965), vol. 140: A1133–A1138 (cit. on p. 5).
6. M. Gell-Mann, K. Brückner: 'Correlation Energy of an Electron Gas at High Density'. *Phys. Rev.* (1957), vol. 106 (cit. on p. 8).
7. J. Perdew, Y. Wang: 'Accurate and simple analytic representation of the electron-gas correlation energy'. *Phys. Rev. B* (1992), vol. 45 (cit. on p. 8).
8. Fiolhais, C., F. Nogueira, and M. A. L. Marques, eds.: *A Primer in Density Functional Theory.* Springer, Berlin, 2003 (cit. on p. 8).
9. Blöchl, P. E.: 'Projector augmented-wave method'. *Phys. Rev. B* (1994), vol. 50: pp. 17953–17979 (cit. on p. 10).
10. Blöchl, P. E. and J. Schimpl C. J. Först: 'The Projector Augmented Wave Method: ab initio molecular dynamics with full wave functions'. *Bull. Mater. Sci.* (2003), vol. 26: pp. 33–41 (cit. on p. 10).
11. Kresse, G. and J. Hafner: 'Ab initio molecule dynamics for liquid metals'. *Phys. Rev. B* (1993), vol. 47: pp. 558–561 (cit. on pp. 12, 17).
12. Kresse, G. and J. Hafner: 'Ab initio molecular-dynamics simulation of the liq-metal-amorphous-semiconductor transistion in germanium'. *Phys. Rev. B* (1994), vol. 49: p. 14251 (cit. on pp. 12, 17).

13. Kresse, G. and J. Furthmüller: ‘Efficiency of ab-initio total energy calculations for metals and semiconductors using a plane-wave basis set’. *Comput. Mater. Sci.* (1996), vol. 6: pp. 15–20 (cit. on pp. 12, 17).
14. Perdew, J. P., K. Burke, and M. Ernzerhof: ‘Generalized Gradient Approximation Made Simple’. *Phys. Rev. Lett.* (1996), vol. 77: pp. 3865–3868 (cit. on p. 12).
15. Tkatchenko, Alexandre and Matthias Scheffler: ‘Accurate Molecular Van Der Waals Interactions from Ground-State Electron Density and Free-Atom Reference Data’. *Phys. Rev. Lett.* (2009), vol. 102: p. 073005 (cit. on p. 12).
16. David Sholl, Janice A Steckel: *Density Functional Theory: A Practical Introduction.* John Wiley & Sons, 2009 (cit. on p. 13).
17. Haken, H. and H.C. Wolf: *The Physics of Atoms and Quanta: Introduction to Experiments and Theory.* Ed. by Physics, Advanced Texts in. Springer, 2005 (cit. on p. 13).
18. Feibelman, P. J. and D. E. Eastman: ‘Photoemission spectroscopy - Correspondence between quantum theory and experimental phenomenology’. *Phys. Rev. B* (1974), vol. 10: p. 4932 (cit. on p. 14).
19. Puschnig, Peter, Stephen Berkebile, Alexander J. Fleming, Georg Koller, Konstantin Emtsev, Thomas Seyller, John D. Riley, Claudia Ambrosch-Draxl, Falko P. Netzer, and Michael G. Ramsey: ‘Reconstruction of Molecular Orbital Densities from Photoemission Data’. *Science* (2009), vol. 326: pp. 702–706 (cit. on p. 14).
20. Hüfner, Stefan: *Photoelectron Spectroscopy.* Springer, Berlin, 2003 (cit. on p. 15).
21. Dauth, M., M. Wiessner, V. Feyer, A. Schöll, P. Puschnig, F. Reinert, and S. Kümmel: ‘Angle resolved photoemission from organic semiconductors: orbital imaging beyond the molecular orbital interpretation’. *New J. Phys.* (2014), vol. 16: p. 103005 (cit. on p. 15).
22. https://cms.mpi.univie.ac.at (cit. on p. 17).
23. https://www.vasp.at (cit. on p. 17).
24. Tao, Y., H. Mao, H. Zhang, and P. He: ‘Electronic properties and adsorption structures of tetracene on the Ag(110) surface’. *Surf. Sci.* (2015), vol. 641: pp. 135–140 (cit. on pp. 18, 19, 43).
25. Chen, Q., A. J. McDowall, and N. V. Richardson: ‘Ordered Structures of Tetracene and Pentacene on Cu(110) Surfaces’. *Langmuir* (2003), vol. 19: pp. 10164–10171 (cit. on pp. 20, 43).
26. Dou Wei-Dong, Zhang Han-Jie and Bao Shi-Ning: ‘Density functional theory calculations of tetracene on low index surfaces of copper crystal’. *Chinese Physics B* (2009), vol. 18: p. 344 (cit. on pp. 20, 43).
27. X. Yang, S. Soubatch: ‘unpublished data’ (cit. on pp. 23, 25, 27, 35, 36, 38–40, 42).

28. Lüftner, D., P. Hurdax, G. Koller, P. Puschnig, M. Ramsey, S. Weiss, X. Yang, S. Soubatch, F. Tautz, V. Feyer, and A. Gottwald: 'Understanding the photoemission distribution of strongly interacting two-dimensional overlayers'. *Phys. Rev. B* (2017), vol. 96: p. 125402 (cit. on p. 24).

29. Schlesinger, Raphael: *Energy-Level Control at Hybrid Inorganic/Organic Semiconductor Interfaces.* Springer International Publishing, 2017 (cit. on p. 30).

30. Heimel, G., L. Romaner, J.-L. Bredas, and E. Zojer: 'Interface Energetics and Level Alignment at Covalent Metal-Molecule Junctions: π-Conjugated Thiols on Gold'. *Phys. Rev. Lett.* (2006), vol. 96: p. 196806 (cit. on p. 30).

31. Willenbockel, M., D. Lüftner, B. Stadtmüller, G. Koller, C. Kumpf, P. Puschnig, S. Soubatch, M. G. Ramsey, and F. S. Tautz: 'The interplay between interface structure, energy level alignment and chemical bonding strength at organic-metal interfaces'. *Phys. Chem. Chem. Phys.* (2015), vol. 17: pp. 1530–1548 (cit. on p. 31).

32. Udhardt, Christian, Felix Otto, Christian Kern, Daniel Lüftner, Tobias Huempfner, Tino Kirchhuebel, Falko Sojka, Matthias Meissner, Bernd Schröter, Roman Forker, Peter Puschnig, and Torsten Fritz: 'Influence of Film and Substrate Structure on Photoelectron Momentum Maps of Coronene Thin Films on Ag(111)'. *Journal of Physical Chemistry* (2017), vol. 121: pp. 12285–12293 (cit. on p. 40).

List of Figures

2.1 Self-consistent solution of Kohn-Sham equations 10
2.2 Schematic illustration of the augmentation region (red) and the interstitial region (blue) 10
2.3 Slab model: side view of 2 supercells 12
2.4 Schematic illustration of photoemission spectroscopy 13
2.5 Schematic illustration of the one-step model (from [20]) 15

3.1 Relaxed super cells for the tetracene/Ag(110) interface, *left*: $\boldsymbol{A}_\perp$, *right*: $\boldsymbol{A}_\parallel$ 19
3.2 Side view of the relaxed supercells for the tetracene/Ag(110) interface, *left*: $\boldsymbol{A}_\perp$, *right*: $\boldsymbol{A}_\parallel$ 20
3.3 Relaxed supercells for the tetracene/Cu(110) interface, *left*: $\boldsymbol{A}_1$, *right*: $\boldsymbol{A}_2$. 21
3.4 Different adsorption sites of tetracene on the Cu(110) surface 22
3.5 Side view of two relaxed supercells for the tetracene/Cu(110) interface, *left*: $\boldsymbol{A}_1$ in long bridge site, *right*: $\boldsymbol{A}_2$ in long bridge site 23
3.6 pDOS of the $\boldsymbol{A}_\parallel$ and the $\boldsymbol{A}_\perp$ tetracene/Ag(110) interface in comparison with the EDC from experiment [27] 25
3.7 Comparison of mopDOS and pDOS for (a) $\boldsymbol{A}_\perp$ and (b) $\boldsymbol{A}_\parallel$ adsorption geometry for the tetracene/Ag(110) system 26
3.8 Comparison of mopDOS, pDOS and experimental EDC [27] for the tetracene/Cu(110) system 27
3.9 Comparison of mopDOS to pDOS for the tetracene/Cu(110) system in (a) the $\boldsymbol{A}_1$ geometry and (b) the $\boldsymbol{A}_2$ geometry 29
3.10 Schematic representation of the push back effect from [29] 30
3.11 Charge density analysis for (a) the $\boldsymbol{A}_\perp$ and (b) the $\boldsymbol{A}_\parallel$ tetracene/Ag(110) interface 32
3.12 Charge density analysis for (a) the $\boldsymbol{A}_1$ and (b) the $\boldsymbol{A}_2$ tetracene/Cu(110) interface 34
3.13 **(a)**: simulated ARPES maps for the $\boldsymbol{A}_\perp$ adsorption geometry, **(b)**: simulated ARPES maps for the $\boldsymbol{A}_\parallel$ adsorption geometry, **(c)**: ARPES maps from experimental data [27] 36
3.14 Side view of the supercells containing a double layer of tetracene on Ag(110), *left*: super cell from Fig. 3.1 right side with an extra layer of tetracene added, *right*: new super cell with a higher coverage 37
3.15 Comparison of the pDOS of the tetracene double layer on Ag(110) (Fig. 3.14, right side) and the experimental EDC [27] 38

3.16 **(a)**: simulated ARPES of a monolayer tetracene on silver, **(b)**: ARPES maps from experimental data [27], **(c)**: simulated ARPES of the upper layer of two layers tetracene on silver, **(d)**: simulated ARPES of the lower layer of two layers tetracene on silver 39
3.17 **(a)**: simulated ARPES maps for tetracene on copper in $\boldsymbol{A}_1$ geometry, **(b)**: ARPES maps from experimental data [27],**(c)**: simulated ARPES maps for tetracene on copper in $\boldsymbol{A}_2$ geometry 40

List of Tables

3.1 Comparison of adsorption energies for different super cells of the tetracene/Ag(110) interface . . . 19
3.2 Comparison of adsorption height for different supercells of the tetracene/Ag(110) interface . . . 20
3.3 Comparison of total energies for different supercells of the tetracene/Cu(110) interface . . . 22
3.4 Comparison of adsorption height for different supercells of the tetracene/Cu(110) interface . . . 22
3.5 Presumed molecular orbital positions from calculated pDOS and experimental EDC for the tetracene/Ag(110) system . . . 25
3.6 Presumed molecular orbital positions from calculated pDOS and experimental EDC for the tetracene/Cu(110) system . . . 27
3.7 Work function variation of the tetracene/Ag(110) system . . . 33
3.8 Work function variation of the tetracene/Ag(110) system . . . 33
3.9 Presumed molecular orbital positions from calculated pDOS for a monolayer and a double layer of tetracene on silver in a parallel adsorption position compared to the experimental EDC [27] . . . 38
3.10 Comparison of adsorption energies for tetracene on Ag(110) and Cu(110) . 41
3.11 Comparison of adsorption height for tetracene on Ag(110) and Cu(110) . . 41
3.12 Comparison of work function variation for tetracene on Ag(110) and Cu(110) 41
3.13 Comparison of the HOMO-LUMO gap for tetracene on Ag(110) and Cu(110) 42